THE GEOLOGICAL SOCIETY OF AMERICA®

Record of coupled hillslope and channel response to Pleistocene erosion and deposition in a sandstone headwater valley, central Pennsylvania

Joanmarie Del Vecchio[1,†], Roman A. DiBiase[1,2], Alison R. Denn[3], Paul R. Bierman[3], M.W. Caffee[4,5], and Susan R. Zimmerman[6]

[1]*Department of Geosciences, Pennsylvania State University, University Park, Pennsylvania 16803, USA*
[2]*Earth and Environmental Systems Institute, Pennsylvania State University, University Park, Pennsylvania 16803, USA*
[3]*Department of Geology, University of Vermont, Burlington, Vermont 05405, USA*
[4]*Department of Physics and Astronomy, Purdue University, West Lafayette, Indiana 47907, USA*
[5]*Department of Earth, Atmospheric, and Planetary Sciences, Purdue University, West Lafayette, Indiana 47907, USA*
[6]*Center for Accelerator Mass Spectrometry, Lawrence Livermore National Laboratory, Livermore, California 94550, USA*

ABSTRACT

We sought to understand the time scale, mechanisms, and extent of landscape modification in unglaciated central Pennsylvania by studying sediment moving through and stored in a sandstone headwater valley. In this landscape, the timing and extent of landscape modification are poorly constrained, and it is unclear whether, and how much, periglacial processes drive landscape evolution during cold glacial periods. Our investigation pairs geomorphic mapping with in situ cosmogenic ^{10}Be and ^{26}Al measurements of surface material and buried clasts to estimate the residence time and depositional history of colluvium within Garner Run, a 1 km^2 headwater valley in the central Appalachian Mountains containing relict Pleistocene periglacial features, including solifluction lobes, boulder fields, and thick colluvial toe-slope deposits. The preservation of periglacial landforms into the present interglacial suggests active hillslope sediment transport in cold climates followed by only limited modification in the Holocene. The ^{10}Be concentrations of stream sediment and hillslope regolith indicate slow erosion rates (6.6 ± 0.6 m m.y.$^{-1}$) over the past ~100 k.y. From ^{26}Al/^{10}Be burial dating of valley-bottom deposits recovered from a 9 m drill core, we infer two pulses of deposition since 340 ± 80 ka, a record that spans at least three glacial terminations and implies limited removal of valley-bottom deposits during interglacial periods. The age of valley-bottom sediment is consistent with independent calculations determined from valley-fill volume estimates, total hillslope contributing area, and the catchment-average erosion rate integrated over multiple climate cycles. We conclude that outside of the Last Glacial Maximum ice margin, landscapes in the central Valley and Ridge physiographic province of eastern North America have experienced extensive periglacial landscape modification. Our study suggests that sandstone headwater valleys preserve soils and thick colluvial deposits that present opportunities for direct examination of the rates and dates of climate-modulated hillslope processes.

INTRODUCTION

Quaternary climate fluctuations profoundly influenced the style and pace of erosion and sedimentation in glaciated landscapes (Hallet et al., 1996; Koppes and Montgomery, 2009), but the extent to which bedrock erosion rates and subsequent sediment transfer in periglacial landscapes were affected by concurrent changes in temperature and hydrology remains unclear. While a switch to colder temperatures is thought to stimulate bedrock lowering through increased frost cracking (Hales and Roering, 2007; Anderson et al., 2013; Rempel et al., 2016), downslope transport of regolith by ice-driven creep, solifluction, and permafrost-thaw mass wasting is more efficient during the periods of warming that follow (Taber, 1929; Matsuoka, 2001; Lewkowicz and Harris, 2005). Additionally, headwater channel networks may be periodically overwhelmed by periglacial hillslope sediment flux (Brush, 1961), insulating these hillslopes from regional base-level change and thus complicating the overall landscape response to changing climate.

In landscapes where erosion rates are slow compared to the frequency of climate shifts, weathering profiles within regolith integrate the effects of multiple glacial-interglacial cycles (Yoo et al., 2011; Anderson et al., 2013). In the central Appalachian Mountains, observations of thick (up to 20 m) packages of colluvium mantling hillslopes and valley floors, often containing buried paleosols, have been interpreted to reflect a complex history of periglacial weathering and sediment transport associated with Pleistocene cold periods (Hoover and Ciolkosz, 1988; Braun, 1989; Ciolkosz et al., 1990; Gardner et al., 1991). Periglacial landscapes like those preserved today in the central Appalachian Mountains were common throughout middle latitudes worldwide during glacial periods (Vandenberghe et al., 2014), but the rates and timing of hillslope response to changing climate conditions are in general poorly constrained. Thus, there is broad importance in understanding the steadiness of surface processes through time and space, and evaluating the impact of past environmental conditions on the composition and structure of the modern surface and shallow subsurface (Anderson et al., 2007; Brantley and Lebedeva, 2011).

In this paper, we quantify the spatial variation of colluvium texture and morphology in a small, structurally controlled, upland basin through detailed surface regolith mapping supplemented by analysis of light detection and ranging (lidar)–derived high-resolution topography. We used the size, shape, and distribution of colluvium on hillslopes and sediment in channels to infer sediment transport processes. To quantify erosion rates and patterns and time scales of hillslope sediment transport, we measured in situ cosmogenic nuclide concentrations in regolith and stream sediment. We also measured in situ cosmogenic ^{10}Be and ^{26}Al concentrations in a valley-bottom sediment core

†joanmarie@psu.edu

GSA Bulletin; November/December 2018; v. 130; no. 11/12; p. 1903–1917; https://doi.org/10.1130/B31912.1; 10 figures; 1 table; Data Repository item 2018099; published online 14 May 2018.

to explore the time scale over which material derived from periglacial hillslope erosion accumulated in the valley bottom. We then discuss implications of time scales of colluvial storage for the long-term evolution of headwater valleys and channels.

STUDY AREA

We focused on Garner Run, a 1 km^2 subcatchment underlain by the Silurian Tuscarora Formation within the Susquehanna Shale Hills Critical Zone Observatory (SSHCZO) in central Pennsylvania (Fig. 1; Brantley et al., 2016). The 150-m-thick Tuscarora Formation is an orthoquartzite sandstone with minor thin interbedded olive-gray shale, and it is overlain in some locations by an upper Castanea Member, an iron-cemented sandstone ~30 m thick (Flueckinger, 1969). Throughout central Pennsylvania, topography primarily reflects Paleozoic structures; the erosion-resistant Tuscarora Formation forms long linear ridges along plunging folds, which typically support the highest topography in the Valley and Ridge Province (Fig. 1). The Garner Run subcatchment lies within a synclinal valley bounded by two linear ridgelines—Tussey Mountain to the northwest, and Leading Ridge to the southeast—and the dip of the Tuscarora Formation parallels, or is slightly steeper than, hillslope topography. Further down valley, the overlying Rose Hill Shale and the Keefer Sandstone crop out in the valley axis (Fig. 1).

Overprinting the lithologic and structural control on topography in central Pennsylvania, there is a regional pattern of contrasting bedrock river steepness that is thought to be associated with a wave of incision propagating up the Susquehanna River basin since the Miocene (Miller et al., 2013). The Garner Run subcatchment lies upstream of a prominent river knickpoint (Fig. 1A), consistent with a temporal change in base level, but it is also coincident with a strong lithologic contrast between the erosion-resistant Tuscarora Formation and more readily eroding overlying rocks (Brantley et al., 2016). Consequently, in the absence of information about erosion rates at Garner Run, the degree to which this and other nearby knickpoints reflect lithologic differences, base-level fall, and/or changes in erosion process is unclear.

Garner Run is located ~75 km south of the Last Glacial Maximum (LGM) Laurentide ice sheet extent at 25 ka (Corbett et al., 2017b), and till deposits indicate that glacial advances remained north of the area in both the Illinoian (ca. 130 ka) and early Pleistocene (ca. 800 ka) glaciations (Ramage et al., 1998; Ciolkosz et al., 2008). In northeastern North America, a cold-climate vegetation assemblage (spruce, fir, and pines) dominated until the end of the Younger Dryas ca. 11 ka, at which point the modern suite of Holocene vegetation (temperate deciduous and warm mixed forests) was established and persisted (Shuman et al., 2002; Williams et al., 2004). Palynological evidence indicates that tundra flora, perhaps in soils underlain by discontinuous or isolated permafrost, persisted in the central Valley and Ridge Province until ca. 16 ka, followed by a transitional period toward alpine communities until they were replaced by the modern hardwood community by 10 ka (Kneller and Peteet, 1999), though cold-climate vegetation communities may have endured longer at higher elevations (Kovar, 1965; Watts, 1979). Peak Holocene summer temperatures did not occur until 7 ka, corresponding to the weakening influence of the receding continental ice sheet and the thermal effects of summer insolation anomalies (Shuman and Marsicek, 2016). The modern climate of Garner Run is temperate (mean annual temperature of 10 °C), with mean annual precipitation of ~1 m (Thomas et al., 2013). Vegetation at present is characterized by deciduous trees with isolated conifers on ridgelines, though the area has been deforested and regrown several times since European settlement in the eighteenth century (Robinson, 1959).

Throughout the central Appalachian Mountains, colluvial deposits indicative of periglacial erosion blanket hillslopes and valley bottoms with blocky debris in areas underlain by resistant sandstone lithologies (Clark et al., 1992), influencing soils and hillslope morphology (Clark and Ciolkosz, 1988; Braun, 1989) as well as fluvial incision (Pizzuto, 1995; Portenga et al., 2013). The preservation of relict landforms today suggests extensive periglacial landscape modification during glacial periods followed by limited and less-effective modification and evacuation of hillslope debris by temperate landscape processes during interglacial periods (Braun, 1989). Like other landscapes in the region, the Garner Run subcatchment contains evidence of extensive periglacial landscape modification during colder climates. Boulder fields and landforms indicative of mass-wasting processes are scattered across hillslopes at Garner Run (Figs. 1 and 2). In the valley axis of Garner Run, a broad, low-sloping bench with subtle lobate terraces suggests significant accumulation of colluvium transported from adjacent hillslopes by mass movements (Merritts et al., 2015; Brantley et al., 2016). Periglacial processes likely played a significant role in regolith generation and sediment transport processes. Catchment-averaged ^{10}Be-derived erosion rates are higher in the Susquehanna River Basin in comparison to the Potomac River Basin to the south, plausibly the result of more-intense periglacial processes adjacent to the LGM ice margin (Portenga et al., 2013). However, both the timing of periglacial modification and the extent of landscape modification during Pleistocene cold periods remain poorly constrained.

METHODS

Topographic Analysis

We used 1-m-resolution lidar-derived topography from both the 2010 leaf-off SSHCZO lidar survey and the 2006 PAMAP lidar survey of Pennsylvania (PAMAP Program, 2006) to generate slope-shade maps for identifying periglacial landforms throughout the Garner Run study catchment and nearby landscape (Fig. 1). We also generated topographic cross sections at Garner Run to estimate the orientation and thickness of the underlying folded bedrock and interpret the thickness of colluvial valley fill, which is additionally constrained by a 9 m core in the valley axis and shallow geophysical surveys (DiBiase et al., 2016).

Field Mapping of Regolith Texture

To characterize spatial variations in regolith surface texture, we mapped boulder density and canopy cover as a proxy for interstitial soil in the field using lidar-derived base maps and sub-meter-resolution global positioning system (GPS) data for positioning. We defined five mapping units based on bedrock exposure, soil and boulder cover, and tree canopy cover: in-place bedrock, showing evidence for original bedding orientation (Fig. 2A); open boulder fields with no soil or tree canopy cover (Fig. 2B); boulder fields with tree canopy, defined by dominant (>67%) surface boulders, which typically lacked a soil matrix and which would shift easily underfoot (Fig. 2C); boulders/soil, defined by abundant (10%–67%) surface boulders that were embedded in soil (Fig. 2D); and soil, defined as mobile regolith with few (<10%) surface boulders (Fig. 2E). We mapped at a resolution of 5 m, which was chosen to balance mapping speed and detail and generally reflects the minimum scale over which regolith texture varied. We digitized field maps in ArcGIS, and for each mapping polygon, we used the lidar topography to determine mean local slope for each polygon. The mean and standard deviation of slope for each surface cover type was then determined from the area-weighted mean and standard deviation of all mapped polygons for each surface cover type.

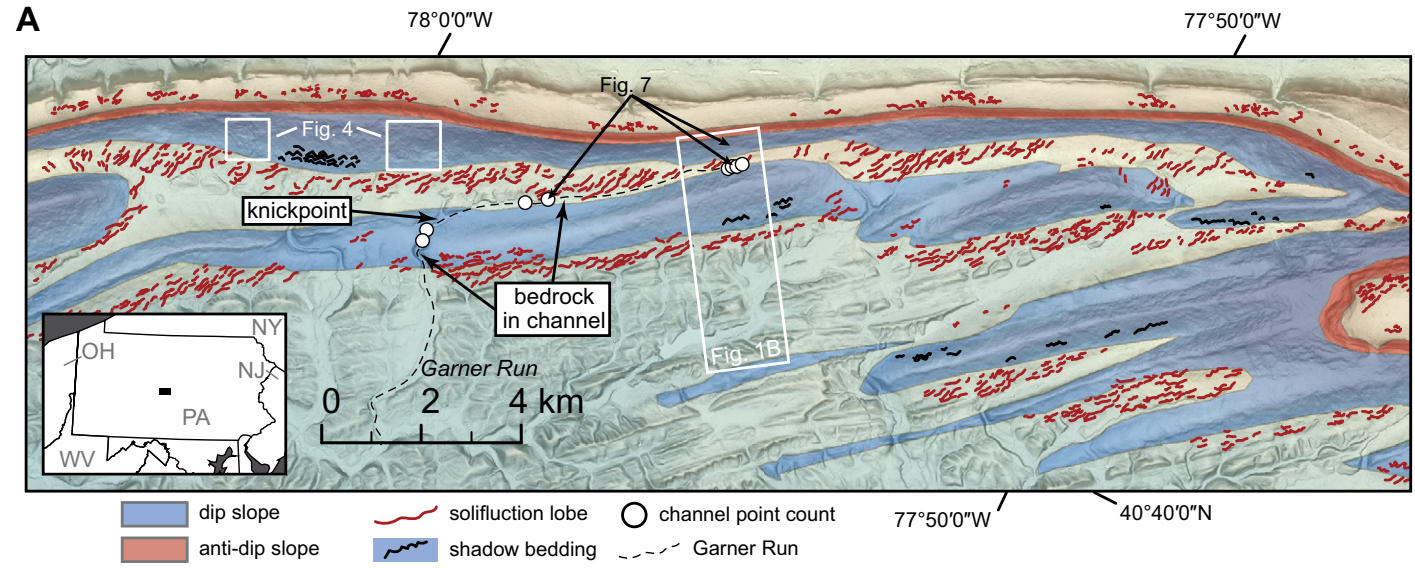

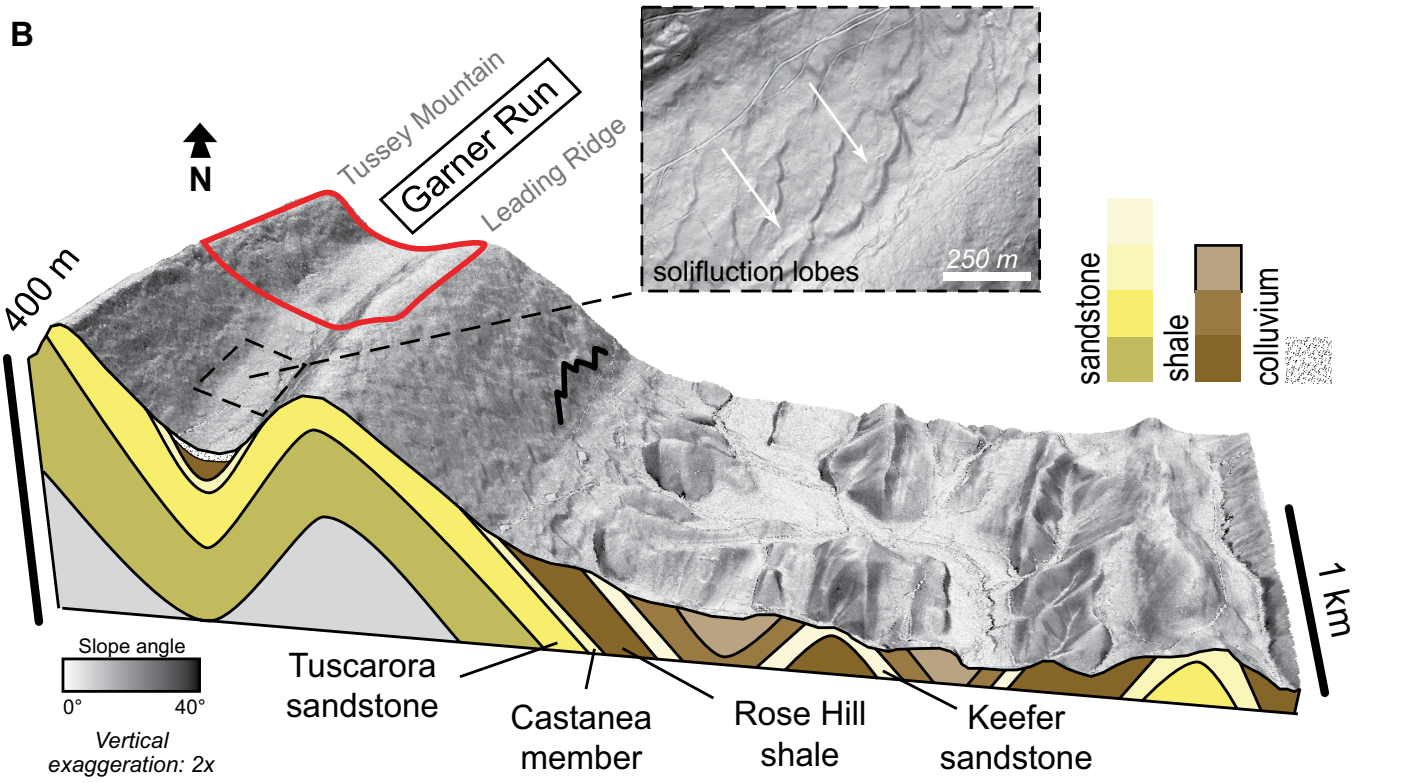

Figure 1. Overview map of Garner Run. (A) Regional topography, showing extent of Tuscarora Formation (blue—dip slopes, red—anti-dip slopes) and location of solifluction lobes (red lines), shadow bedding (black lines), field observations of channel sediment and in-channel bedrock, and knickpoint along Garner Run. Inset shows location of Garner Run in Pennsylvania; white boxes indicates areas shown in Figure 1B and Figure 4. Locations of channel point counts are indicated by white circles. (B) Perspective block diagram showing light detection and ranging (lidar) surface topography slope-shade map and subsurface geology from Flueckinger (1969), highlighting the synclinal valley of Garner Run between Tussey Mountain and Leading Ridge. Shadow bedding on the southeast-facing slope of Leading Ridge is outlined in black, indicating hillslope angle is slightly less than dip of sandstone bedding. Red outline indicates extent of Garner Run subcatchment. Inset map shows detail of solifluction lobes in low-sloping valley floor. Note the obliquity of the apparent lobe motion relative to the downslope direction (white arrows), which is a feature prevalent in solifluction lobes in central Pennsylvania.

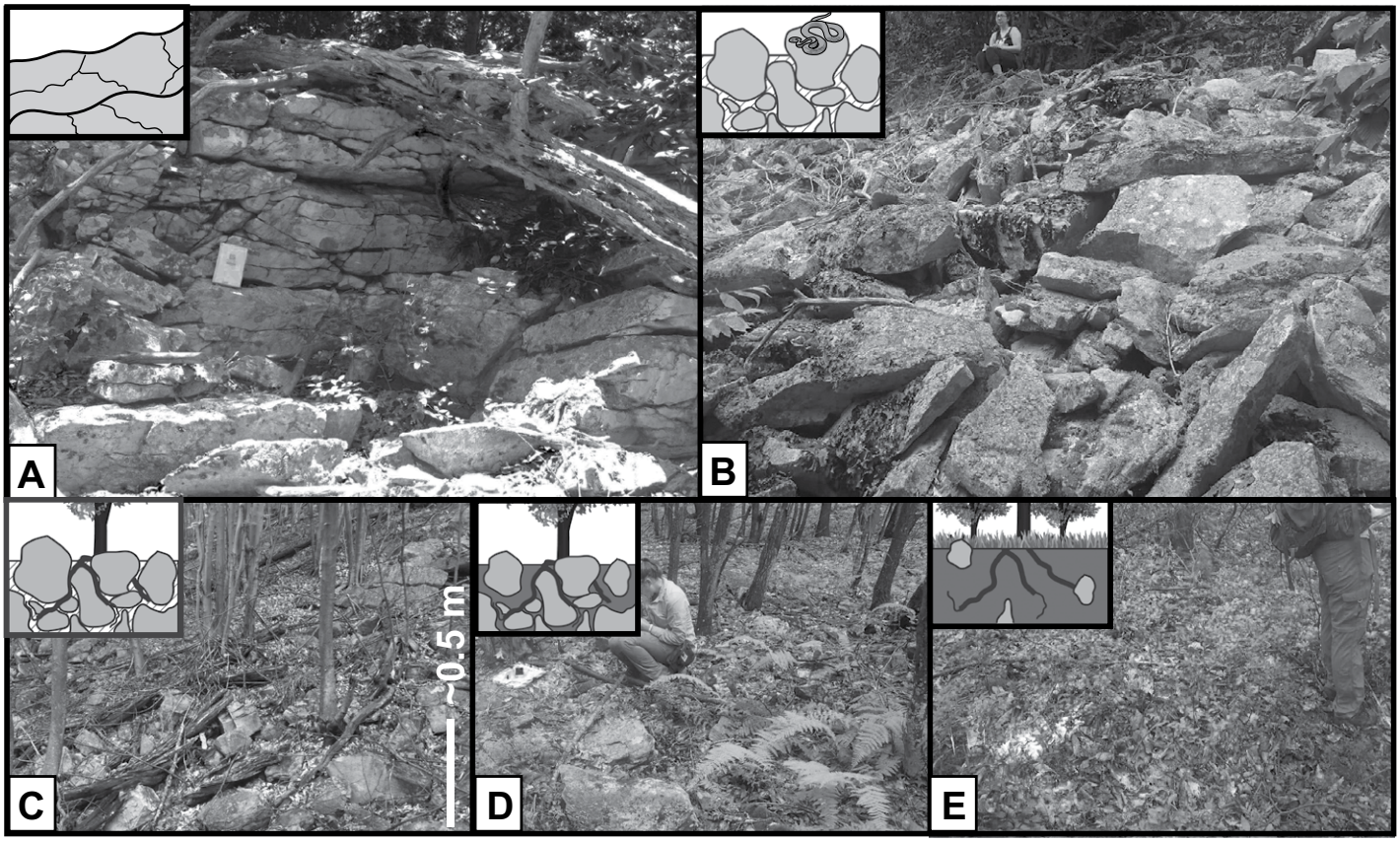

Figure 2. Photographs showing heterogeneity in surface cover. Letters correspond to mapping units in Figure 3. (A) In-place bedrock showing typical Tuscarora sandstone outcrop along ridgeline with visible bedding planes. (B) Open boulder fields devoid of soil and canopy. (C) Canopied boulder fields. (D) Boulders/soil, characterized by boulders embedded within a fine-grained matrix. (E) Soil, characterized by fine-grained regolith mostly devoid of surface boulders. Inset figures show cartoon of subsurface interpretation (bedrock/boulders—light gray; void space—hatched; interstitial soil—dark gray).

We also dug several shallow (<50 cm) soil pits on the different mapping units to examine clasts at depth and their relation to any soil horizons (Fig. DR2[1]), complementing four deeper soil pits along the GroundHOG (Ground Hydrological Observation Gear) transect, a monitoring transect established at Garner Run as part of the SSHCZO (Fig. 3; Brantley et al., 2016).

Analysis of Coarse Surface Clasts on Hillslope and in Channels

We conducted point counts of the intermediate axis of 40–100 surface clasts of at least cobble size (≥6.4 cm) along a 1 m grid at 23 hillslope sites to characterize surface patterns in grain-size distribution (Bunte and Abt, 2001; Fig. DR1 [see footnote 1]). Hillslope sites included all mapped units except for soil-mantled areas with few surface clasts. Both open and canopied boulder fields typically contained no finer-grained material, and thus point counts in these areas reflect the full grain-size distribution of surface regolith. Point counts of coarse sediment on otherwise soil-mantled surfaces ("boulders/soil" mapping classification) do not reflect the full distribution of sediment grain size, and so are not directly comparable to coarse sediment point counts of boulder fields, but nonetheless they provide constraints on maximum boulder size.

At eight locations along the channel in and downstream of the Garner Run subcatchment (Fig. 1A) we conducted similar point counts as on hillslopes; we incorporated all grains within the active channel, defining material with diameter <2 mm as "fine" (Table DR2 [see footnote 1]). Four channel point counts were spaced at ~100 m in the headwaters, beginning with the onset of channelized flow; two point counts were conducted 4 km downstream from the subcatchment; and two point counts were conducted 6 km downstream from the subcatchment, where Garner Run turns southeast and steepens across a knickpoint (Fig. 1A). In addition to grain-size characteristics, observations of any non-sandstone clasts and any bedrock exposed in the stream channel were noted.

To aid in visualization of grain shape, sorting, and organization, we constructed structure-from-motion photogrammetry models (Westoby et al., 2012) of three point count sites using a digital single-lens reflex camera with wide-angle lens. We aligned 50–100 photographs of each site and constructed dense point clouds using Agisoft Photoscan, and we scaled our models using 15 cm rulers scattered throughout the scene. Visualization of dense point clouds was performed using the EyeDome lighting shader in CloudCompare (http://danielgm.net/cc).

Cosmogenic Nuclide Sampling

To quantify the average concentration of in situ–produced cosmogenic ^{10}Be in regolith, we sampled material from the four soil pits monitored as part of the SSHCZO at Garner Run (GroundHOG transect of Brantley et al.,

[1]GSA Data Repository item 2018099, soil pit descriptions, point count data, and cosmogenic nuclide data, Tables DR1–DR3, Figures DR1–DR7, is available at http://www.geosociety.org/datarepository/2018 or by request to editing@geosociety.org.

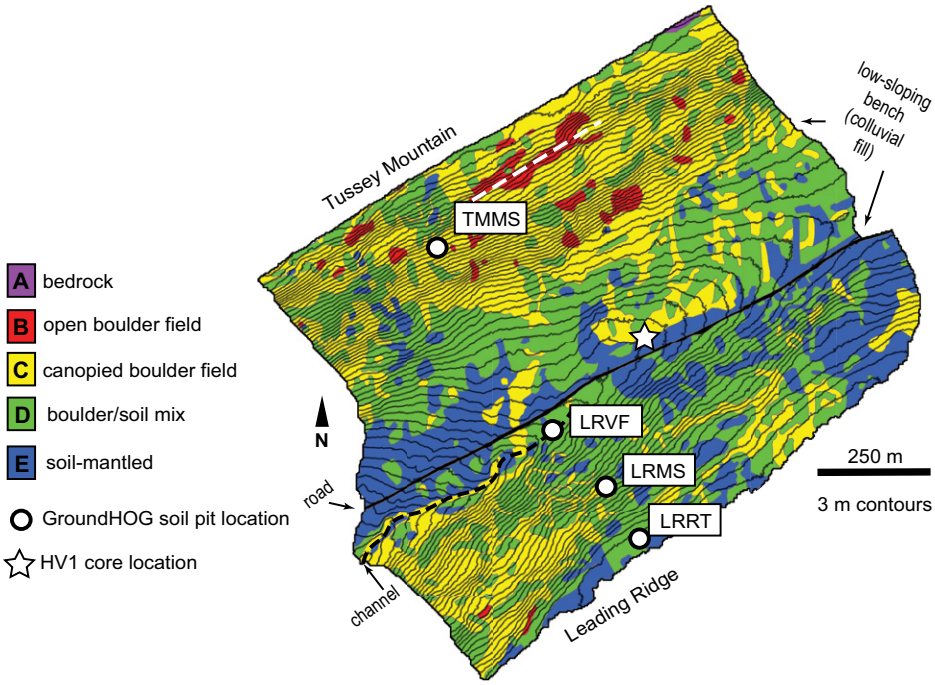

Figure 3. Surface regolith texture map of Garner Run, highlighting patterns in boulder and soil cover and location of GroundHOG soil pits and the HV1 drill core. Photographs and descriptions of mapping units are shown in Figure 2. Black dashed line indicates channel of Garner Run, which flows to the southwest. Solid black line indicates road. White dashed line on Tussey Mountain hillslope highlights linear pattern in boulder occurrences. TMMS—Tussey Mountain midslope; LRVF—Leading Ridge valley floor; LRMS—Leading Ridge midslope; LRRT—Leading Ridge ridgetop.

2016). Three soil pits were located along the north-facing slope of Leading Ridge, and one was on the south-facing slope of Tussey Mountain (Fig. 3). These pits were dug to different depths—to 0.7 m on the Tussey Mountain midslope (TMMS), to 0.65 m on the Leading Ridge ridgetop (LRRT), to 1.4 m on the Leading Ridge midslope (LRMS), and to 1.4 m on the Leading Ridge valley floor (LRVF)—based on the depth of refusal (Brantley et al., 2016). Although the depth to bedrock is not known, pit bottoms contained firm material that could not be excavated by hand; each pit likely integrates a large portion of the total mobile regolith profile (Jungers et al., 2009). We amalgamated 100 g of material from each identified soil horizon for a given soil pit and sieved amalgamated horizon material to the 250–850 µm fraction sampled within the soil profile, creating a single sample for each soil pit (see the Data Repository material [footnote 1]).

We sampled surface boulders along three 30-m-long, slope-normal transects adjacent to each of the three soil pits on the north-facing slope of Leading Ridge and analyzed these samples for both ^{10}Be and ^{26}Al (Fig. 3). Every 2 m along each transect we removed the uppermost few centimeters of rock from the nearest boulder, sampling boulders representative of the typical boulder size on the slope (~1 m or less) for a total of 15 boulder chips per transect. Each chip was crushed and sieved individually, and 50 g aliquots of each clast were amalgamated into one sample per transect.

To quantify catchment-averaged erosion rates, we collected two stream sediment samples for in situ–produced cosmogenic ^{10}Be analysis, ~15 m upstream and downstream from the soil pit transect. Samples were sieved in the field to the 250–850 µm fraction.

To constrain the burial age and thus history of the colluvial fill in Garner Run, we measured in situ–produced cosmogenic ^{10}Be and ^{26}Al in three buried clasts recovered from a 9.1 m-deep drill core in the valley axis of Garner Run, just upstream from the soil pit transect (Fig. 3; Brantley et al., 2016; DiBiase et al., 2016). Material recovered during drilling (performed using a Hydracore Prospector) consisted of discontinuous sandstone clasts dispersed throughout iron-stained sandy fill from four known depth intervals. Two sandstone clasts were recovered between 0 and 3.3 m, but their relative depths were not recorded. Five clasts, totaling 40 cm of competent cored material, were recovered in order from depths of 3.4–4.8 m, and four clasts totaling 50 cm of core were recovered in order from depths of 4.8–6.4 m. Only sand was present at depths of 6.4–9.1 m. We sampled the upper clast recovered in the 3.4–4.8 m interval and the uppermost and lowermost clasts recovered from the 4.8–6.4 m interval. Because the cores were logged in order of recovery rather than at discrete depths, we conservatively assigned depths and uncertainty based on the order and length of cored clasts, resulting in depths of 3.9 ± 0.5 m, 5.3 ± 0.5 m, and 5.9 ± 0.5 m for GR10, GR11, and GR12, respectively.

Cosmogenic Nuclide Sample Analysis and Data Reduction

For all samples, we purified quartz by heating the ground and/or sieved samples in HCl and treating them with a series of leaches using dilute HF/HNO_3 mixtures at the University of Vermont Cosmogenic Nuclide Laboratory (Kohl and Nishiizumi, 1992). We extracted ^{10}Be from all samples, and ^{26}Al from some samples, following the methods of Corbett et al. (2016). All Garner Run samples were analyzed for ^{10}Be at the Center for Accelerator Mass Spectrometry (CAMS) at Lawrence Livermore National Laboratory, normalizing measured ratios to ICN standard 07KNSTD3110 with an assumed value of 2.85×10^{-12} (Nishiizumi et al., 2007). Samples GR01–GR09 were analyzed in April 2016, and GR10–GR12 were analyzed in July 2016. We background-corrected samples using an average of $n = 3$ process blanks (^{10}Be/^{9}Be = $1.20 \pm 0.66 \times 10^{-15}$). For the drill core samples ($n = 3$) and the amalgamated surface boulder transect samples ($n = 3$), we also measured ^{26}Al at the Purdue Rare Isotope Measurement (PRIME) Laboratory. Sample ratios for ^{26}Al were normalized to standard KNSTD with an assumed ratio of 1.818×10^{-12} (Nishiizumi, 2004) and background corrected using an average of $n = 3$ process blanks (^{26}Al/^{27}Al = $1.97 \pm 0.98 \times 10^{-14}$).

The samples GR08 and GR10 were each run twice, the ^{10}Be at CAMS (second run March 2017) and the ^{26}Al at PRIME Laboratory (second run April 2017). Although other sample replicate runs were within 1σ error of the original runs, the ^{26}Al analyses for sample GR08 differed by ~3σ. The sample GR08 had more Mg isobaric interference (870 counts per second [cps]) than others analyzed at that time (20–570 cps), which could have resulted in an elevated ^{26}Al/^{27}Al ratio; Mg counts could have the same energy loss characteristics as ^{26}Al and therefore add to measured ^{26}Al. Samples with 370 cps of Mg on the same run had very low ^{26}Al/^{27}Al ratios (1×10^{-15}), so we consider it unlikely as the cause of the disparity, and thus we cannot justify disregarding the initial analysis of GR08. We accordingly report the average value and

standard error (n = 2) for each of the two replicated samples in our analysis.

Minimum limiting exposure ages and maximum limiting erosion rates were calculated using the CRONUS-Earth online calculator (http://hess.ess.washington.edu/, wrapper script 2.3, main calculator 2.1, constants 2.2.1; see Balco et al., 2008) based on the constant production rate model (Lal, 1991; Stone, 2000; Table DR1 [see footnote 1]).

Determining Colluvial-Fill History

As a first-order constraint on the age of colluvial fill in Garner Run, we divided colluvial-fill volume in the valley axis by the average hillslope lowering rates on the adjacent steeply dipping slopes determined from ^{10}Be concentrations in stream sediment (samples GR01 and GR02). To determine colluvial-fill volume, we constructed a series of topographic cross sections from Tussey Mountain to Leading Ridge (Fig. 1). We estimated the boundary between fill and bedrock based on surface topography and core depth, which is consistent with estimates from shallow geophysical surveys (DiBiase et al., 2016). We assumed constant regolith storage on hillslopes over the period of valley filling, a colluvium density of 1600 kg m^{-3}, and a bedrock density of 2700 kg m^{-3}, and we assumed that the contributing area of sediment production was limited to the steeply dipping slopes, which cover ~75% of the catchment area (Fig. 1B).

To evaluate potential colluvial valley-fill histories consistent with cosmogenic radionuclide ratios measured in the core, we modeled the production and decay of in situ cosmogenic ^{10}Be and ^{26}Al in a one-dimensional (1-D), 6.5-m-thick colluvial fill for three scenarios: a single burial event, gradual burial, and pulsed burial.

For the single burial event scenario, we modeled the in situ production and radioactive decay of ^{10}Be and ^{26}Al as a function of depth below the modern surface, z, for burial ages, t_0, ranging from 50 to 400 ka (e.g., Granger and Muzikar, 2001):

$$N_{10Be}(z,t_0) = N_{10Be}^{inh}\exp(-\lambda_{10Be}t_0) + P_{10Be}(z)\left(\frac{1-\exp(-\lambda_{10Be}t_0)}{\lambda_{10Be}}\right), \quad (1a)$$

$$N_{26Al}(z,t_0) = N_{26Al}^{inh}\exp(-\lambda_{26Al}t_0) + P_{26Al}(z)\left(\frac{1-\exp(-\lambda_{26Al}t_0)}{\lambda_{26Al}}\right), \quad (1b)$$

where N_{10Be} and N_{26Al} are the modern concentrations of ^{10}Be and ^{26}Al, respectively, N_{10Be}^{inh} and N_{26Al}^{inh} are the inherited concentrations of ^{10}Be and ^{26}Al, respectively, λ_{10Be} and λ_{26Al} are the decay constants for ^{10}Be and ^{26}Al, respectively, and P_{10Be} and P_{26Al} are the depth-dependent postburial production rates of ^{10}Be and ^{26}Al, respectively, which we characterize as:

$$P_{10Be}(z) = P_{10Be}^{spall}(0)\exp\left(\frac{-\rho z}{\Lambda_{spall}}\right) + P_{10Be}^{muon}(0)\exp\left(\frac{-\rho z}{\Lambda_{muon}}\right), \quad (2a)$$

$$P_{26Al}(z) = R_{26/10}P_{10Be}(z), \quad (2b)$$

where $P_{10Be}^{spall}(0)$ and $P_{10Be}^{muon}(0)$ are the local surface production rate of ^{10}Be due to neutron spallation and negative muon capture, respectively, ρ is the bulk density of colluvial fill, Λ_{spall} and Λ_{muon} are the mass attenuation lengths for neutron spallation and negative muon capture, respectively, and $R_{(26/10)}$ is the production rate ratio for ^{26}Al and ^{10}Be. We assumed production due to fast muons was negligible at depths less than 10 m (Granger and Riebe, 2014).

For the gradual burial scenario, we modeled steady accumulation of material at a 500 yr time step from an initial time, t_0, to the present, with t_0 varying from 50 to 400 ka (corresponding to accumulation rates of 2–13 cm k.y.$^{-1}$); we also tracked postburial production and decay following Equations 1 and 2.

For the pulsed burial event scenario, we modeled an initial depositional event at time t_0, followed by a hiatus and a second depositional event at time t_1. The timing and thickness of each event were adjusted based on constraints from both the ^{10}Be concentration and ^{26}Al/^{10}Be ratio of the three buried core samples.

For each scenario, we assumed a uniform inherited ^{10}Be concentration, N_{10Be}^{inh}, based on the mean ^{10}Be concentration measured from the three amalgamated surface boulder transects (GR07–GR09), although the inheritance varies among individual clasts (see the Data Repository material [footnote 1]). We assumed an inherited ^{26}Al/^{10}Be ratio (and thus a value for N_{26Al}^{inh}) based on the mean ratio measured from the same amalgamated surface boulder transects, which may vary from the actual production rate ratio due to burial and preferential decay of ^{26}Al during downslope transport or because of differences in the subsurface attenuation length of ^{10}Be and ^{26}Al production (Argento et al., 2015). Postburial production of ^{10}Be by neutron spallation and negative muon capture was modeled assuming a spallation attenuation length scale for both isotopes of Λ_{spall} = 160 g cm^{-2}, and a negative muon capture attenuation length scale of Λ_{muon} = 1000 g cm^{-2} (Granger and Riebe, 2014). We assumed a colluvial-fill bulk density of ρ = 1.6 g cm^{-3}, based on typical values for sandy soils (Soil Survey Staff, 2014). The surface production rate of ^{10}Be for both spallation ($P_{10Be}^{spall}(0)$) and negative muon capture ($P_{10Be}^{muon}(0)$) was determined using the CRONUS-Earth online calculator (http://hess.ess.washington.edu/, wrapper script 2.2, main calculator 2.1, constants 2.2.1; see Balco et al., 2008).We determined the ^{26}Al production rate, $P_{26Al}(z)$, based on an assumed ^{26}Al/^{10}Be production rate ratio of $R_{(26/10)}$ = 6.75 (Balco et al., 2008), but we show results from ratios $R_{(26/10)}$ = 6.5 and $R_{(26/10)}$ = 7.0 in the Data Repository for comparison (see footnote 1; Corbett et al., 2017a). Radioactive decay for ^{10}Be and ^{26}Al was modeled assuming half-lives of 0.705 m.y. (Nishiizumi, 2004) and 1.387 m.y. (Chmeleff et al., 2010), respectively, corresponding to decay constants of Λ_{26Al} = 5.00 × 10^{-7} yr^{-1} and Λ_{10Be} = 9.83 × 10^{-7} yr^{-1}.

RESULTS

Topographic Analysis

Lidar-derived topographic data indicate that gradients of Tuscarora Formation hillslopes mirror those of the underlying structure of plunging folds throughout central Pennsylvania, except where anticlines are breached (Fig. 1A). Within the Garner Run subcatchment, the south-facing planar hillslopes of Tussey Mountain maintain nearly constant gradient and orientation, whereas the north-facing slopes of Leading Ridge steepen with distance down valley in concert with changing fold geometry. Throughout the region, subtle cuestas (dip slopes conforming to underlying resistant bedrock) on the south-facing hillslopes appear to show shadow bedding planes dipping slightly steeper than the slope gradient (Fig. 1; Brantley et al., 2016).

In contrast to the near-dip slopes, the southeast-facing toe slope of Tussey Mountain contains a low-sloping bench marked at the surface by lobate structures oriented oblique to the valley axis that we interpret to be solifluction lobes (Fig. 1B). In locations where Garner Run appears to intersect and incise through surface lobes, the channel banks expose colluvial fill up to 5 m thick. This bench widens down valley, and in most places, these lobes have pinned Garner Run to the base of Leading Ridge; where these lobes are less prominent, the channel of Garner Run flows closer to the center of the valley axis (Fig. 1A).

From the lidar slope-shade map, we observed a number of mass movements that we interpret to be slides and slumps in the upper few meters of regolith (Fig. 4; Brantley et al., 2016). These

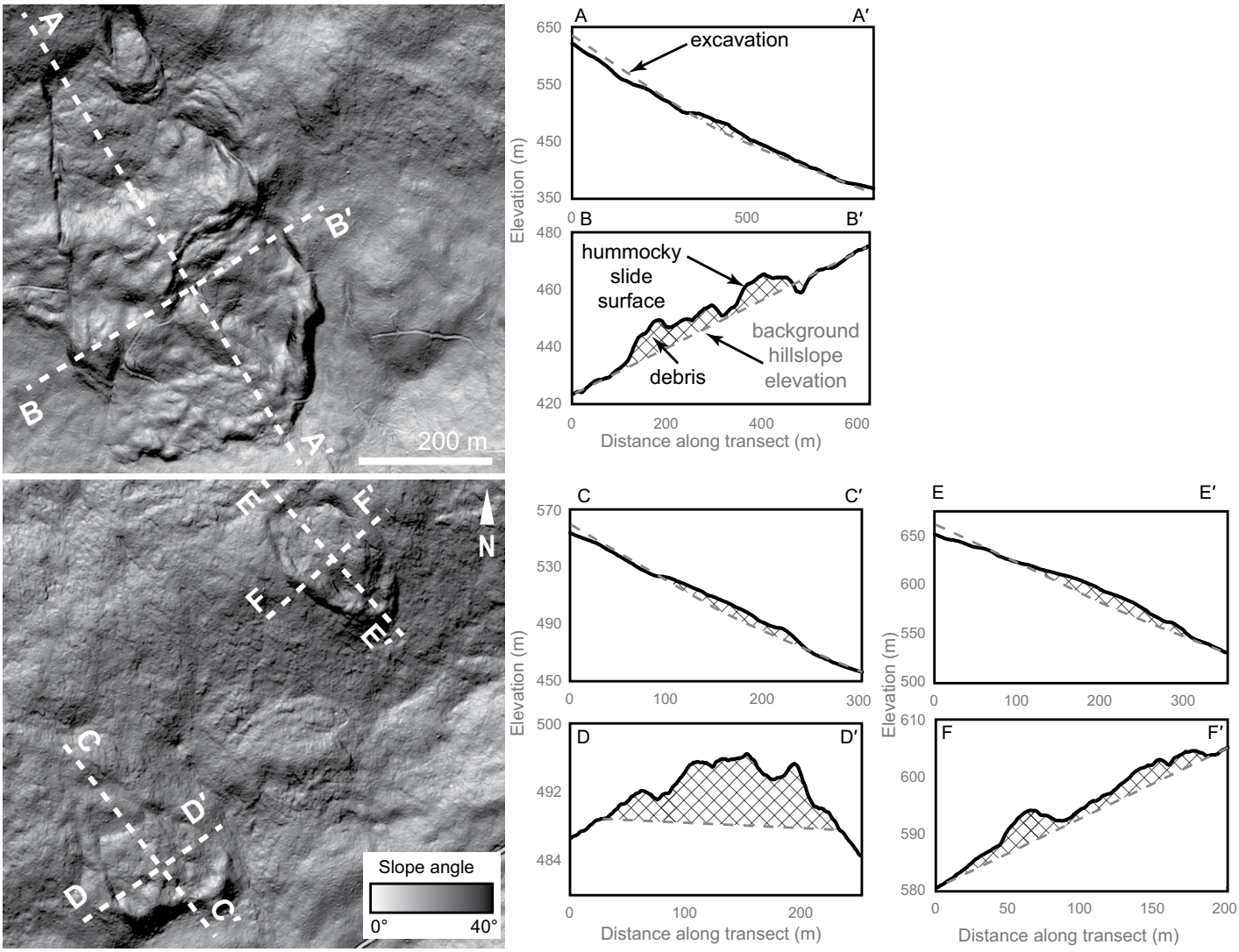

Figure 4. Topographic profiles across slump features along Tussey Mountain, demonstrating the inferred depth of excavation and thickness of debris, which changes topography by 5–10 m compared to background. Solid lines show present topography, whereas dashed gray lines show an interpretation of the planar, dip-slope hillslope prior to failure; the difference between the two profiles shows elevation gain and loss. Location is shown on Figure 1A.

features are tens to hundreds of meters across, and they appear as either angular or curvilinear scars with hummocky landslide deposits downslope. Topographic profiles drawn across these scars indicate that smaller slumps excavated and extruded ~2 m of regolith, while the debris from larger slides is 5–10 m thick (Fig. 4).

Field Mapping of Regolith Texture

In general, much of the central Pennsylvania landscape underlain by the Tuscarora Formation is covered in boulder-rich regolith to varying degrees, with only occasional bedrock exposure along ridgelines (Figs. 2 and 3). In the Garner Run subcatchment, field mapping results show that the southeast-facing slope of Tussey Mountain is generally more boulder-mantled than the northwest-facing slope of Leading Ridge (Fig. 3). At and within 200 m of the ridgeline of Tussey Mountain, boulder fields form a linear pattern trending roughly parallel to the strike of the underlying bedrock (Fig. 3). The area-weighted mean, and standard deviation in local slope of individual polygons mapped as open boulder fields is 21.8° ± 2.4°. Areas of the hillslope mapped as canopied boulder field and boulder/soil mix have local slopes of 15.0° ± 3.7° and 11.5° ± 4.0°, respectively. Soil-mantled areas lacking boulders have local slopes of 8.5° ± 3.2° and are largely confined to the low-sloping valley floor and the northeastern flank of Leading Ridge (Fig. 3). Within the valley floor, lobes tend to be flanked by boulders but are soil-mantled on top. Downstream of the Garner Run subcatchment, where solifluction lobe crests become more prominent (Fig. 1B), incision into the colluvial valley fill exposes coarse blocky debris overlain by fine-grained material that blankets the entire topographic bench.

Shallow soil pits showed that, on the south-facing dip slope of Tussey Mountain, a gray E horizon up to 15 cm thick occurs between the O/A horizons and a red, clay-rich B horizon (see the Data Repository [footnote 1]). However, this soil horizon thins in sites downslope and disappears completely at sites in the valley floor. The material mantling the low-sloping bench consists of mainly soil or a boulder/soil mix and

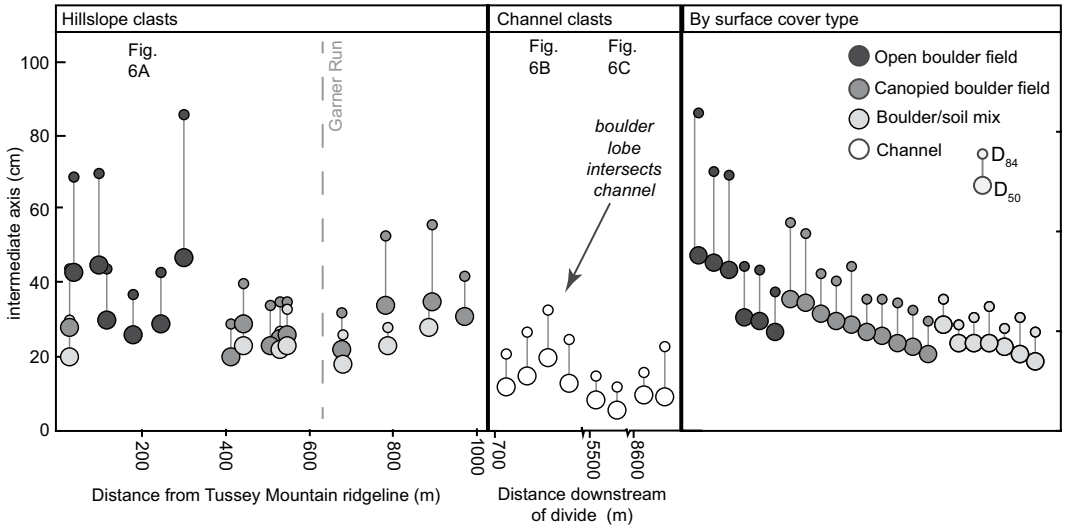

Figure 5. Clast measurements from hillslope and channel point counts, showing D_{50} (large circles) and D_{84} (smaller circles) at point count locations and shaded by surface cover type. Arrow points to site where solifluction lobe intersects stream, reflected as larger grain size at survey site. Labels indicate approximate locations of structure-from-motion models shown in Figure 6. Locations of channel and hillslope point counts are shown in Figure 1A and Figure DR1 (see text footnote 1), respectively. Right panel shows same data sorted by cover type.

exhibits a clayey B horizon just below the surface. Shallow excavations (0.5–1.0 m) of rocky areas revealed that surficial rocks corresponded to rocks at depth, and boulders were embedded within both E and B horizons.

Analysis of Coarse Surface Clasts on Hillslopes and in Channels

On the hillslopes in the Garner Run subcatchment, the largest grains (intermediate axes > 0.7 m) are generally restricted to boulder fields near ridgelines and the toe slope of Tussey Mountain (Fig. DR1 [see footnote 1]). The median and 84th percentile of intermediate axes of clasts in canopied and open boulder fields are also generally larger than those embedded in a soil matrix, regardless of hillslope position (Fig. 5). Clasts in open boulder fields are angular, while clasts in canopied boulder fields and those in a soil matrix tend to be subangular. Most clasts are tabular and rarely exceed 25 cm in thickness. Within a given surface cover type, we observed a general decrease in median surface clast size with distance downslope for both Tussey Mountain and Leading Ridge hillslopes (Fig. 5; see the Data Repository [see footnote 1]). Median intermediate axis diameter ranged from a high of D_{50} = 47 cm in open boulder fields on the Tussey Mountain hillslope to a low of D_{50} = 18 cm in the valley floor where interstitial soil was prevalent.

Within the Garner Run subcatchment, the median grain size of streambed sediment at four locations (D_{50} = 12, 13, 15, and 20 cm) tended to be slightly finer than the surface clasts in boulder fields and boulder/soil near the valley floor (D_{50} = 18–23 cm), but with similar shape and angularity (Fig. 6). The channel site with the coarsest surface material (D_{50} = 20 cm) is directly adjacent to a boulder-lined lobe that feeds into the channel from Tussey Mountain (Fig. 3). Downstream of the Garner Run subcatchment, channel sediment shows evidence of sorting and rounding and decreases in grain size (D_{50} = 6–10 cm; Figs. 5 and 6). Additionally, the colluvial valley fill thins, as evidenced by bedrock exposure of the Rose Hill Shale in the channel floor (Fig. 1A). Further downstream, where the channel steepens and turns south across a knickpoint, coarse material again emerges in the channel coincident with steeper hillslopes located adjacent to channel banks (Fig. 5).

Cosmogenic Nuclide Analysis

Measured surface ^{10}Be concentrations at Garner Run range from 2 to 8 × 10^5 atoms g^{-1}, with depth-integrated soil samples, amalgamated surface boulder samples, and stream sediment samples having broadly similar concentrations (Table 1; Fig. 7). The ^{10}Be concentrations in depth-integrated soil pit samples (n = 3) from the northwest-facing slope of Leading Ridge increase downslope, but ^{10}Be concentrations in amalgamated surface boulder samples show no

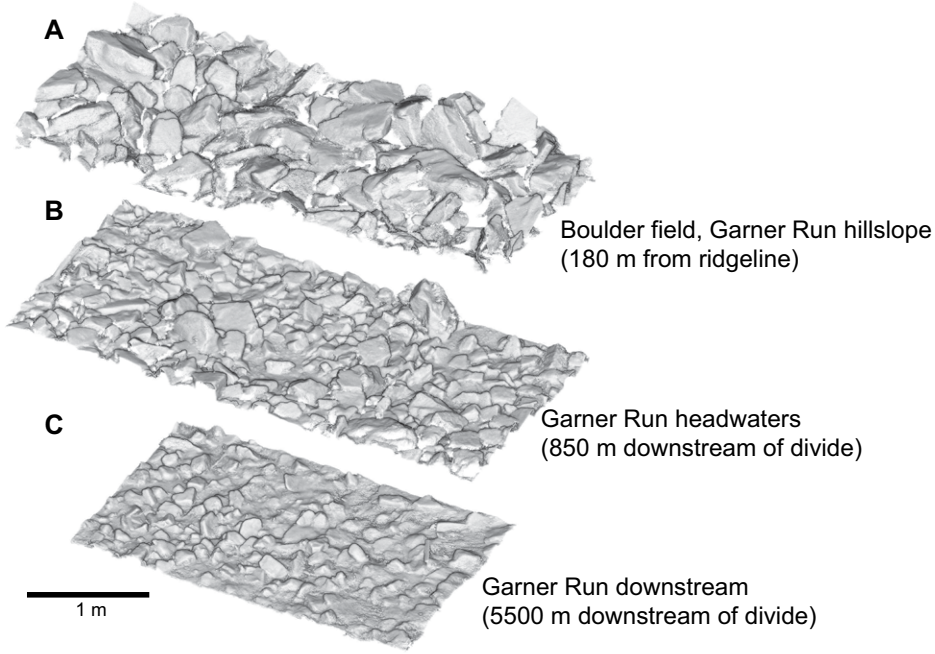

Figure 6. Perspective views of surface topography generated using structure-from-motion photogrammetry, highlighting differences in clast size, shape, and sorting between (A) open boulder field (Fig. 2B); (B) headwater channel; and (C) channel bed ~5 km downstream of B.

TABLE 1. ISOTOPIC DATA FOR GARNER RUN STREAM, SLOPE, AND CORE SAMPLES

Batch	Sample ID	Sample location, type	Latitude*	Longitude*	Elevation (m asl)	Depth§ (m)	^{10}Be production# Spallogenic (atoms g^{-1} yr^{-1})	^{10}Be production# Muonogenic (atoms g^{-1} yr^{-1})	Quartz (g)	^{9}Be (µg)	Blank corrected ^{10}Be/^{9}Be††,§§	Blank corrected ±##
573	GR01	Stream, upstream	40.6961	–77.9213	559†	ND	6.23	0.091	20.10	248.3	7.99×10^{-13}	1.15×10^{-14}
573	GR02	Stream, downstream	40.6959	–77.9217	559†	ND	6.23	0.091	20.07	248.3	6.40×10^{-13}	7.45×10^{-15}
573	GR03	TMMS, soil	40.6997	–77.9246	575	ND	6.26	0.091	20.08	248.1	9.60×10^{-13}	1.66×10^{-14}
573	GR04	LRRT, soil	40.6939	–77.9190	586	ND	6.32	0.092	10.19	248.3	1.77×10^{-13}	3.46×10^{-15}
573	GR05	LRMS, soil	40.6949	–77.9199	555	ND	6.15	0.091	20.05	247.4	4.96×10^{-13}	6.59×10^{-15}
573	GR06	LRVF, soil	40.6959	–77.9214	526	ND	6.00	0.090	20.39	247.4	1.02×10^{-12}	1.68×10^{-14}
573	GR07	LRRT, rock	40.6939	–77.9190	586	ND	6.32	0.092	20.26	246.8	4.11×10^{-13}	1.00×10^{-14}
573	GR08	LRMS, rock	40.6949	–77.9199	555	ND	6.15	0.091	20.25	247.5	2.77×10^{-13}	3.40×10^{-15}
591	GR08Rep	LRMS, rock				ND			14.34	247.0	1.90×10^{-13}	2.60×10^{-15}
573	GR09	LRVF, rock	40.6959	–77.9214	526	ND	6.00	0.090	21.83	247.8	8.42×10^{-13}	9.60×10^{-15}
582	GR10	Core, top	40.6978	–77.9190	529	3.9 ± 0.5	6.00	0.090	22.53	247.0	1.19×10^{-12}	2.00×10^{-14}
591	GR10Rep	Core, top							10.04	245.7	5.27×10^{-13}	6.34×10^{-15}
582	GR11	Core, middle	40.6978	–77.9190	529	5.3 ± 0.5	6.00	0.090	17.21	246.5	5.26×10^{-13}	1.00×10^{-14}
583	GR12	Core, bottom	40.6978	–77.9190	529	5.9 ± 0.5	6.00	0.090	20.83	250.1	1.56×10^{-12}	3.38×10^{-14}

Batch	Sample ID	Concentration ^{10}Be††,§§,## (atoms g^{-1})	±	^{27}Al (µg)	Blank corrected ^{26}Al/^{27}Al***,†††	±	Concentration ^{26}Al§§,***,††† (atoms g^{-1})	±	Ratio ^{26}Al/^{10}Be	±	Erosion rate### (m m.y.$^{-1}$)	±	Exposure age### (yr)	±
573	GR01	6.59×10^{5}	9.47×10^{3}	3003	ND		ND		ND		5.85	0.5	ND	ND
573	GR02	5.29×10^{5}	6.16×10^{3}	2897	ND		ND		ND		7.43	0.62	ND	ND
573	GR03	7.93×10^{5}	1.37×10^{4}	3066	ND		ND		ND		ND	ND	129,000	11,600
573	GR04	2.89×10^{5}	5.64×10^{3}	5453	ND		ND		ND		ND	ND	45,800	4000
573	GR05	4.09×10^{5}	5.43×10^{3}	2800	ND		ND		ND		ND	ND	66,700	5900
573	GR06	8.26×10^{5}	1.37×10^{4}	2837	ND		ND		ND		ND	ND	140,400	12,700
573	GR07	3.35×10^{5}	8.17×10^{3}	6308	3.13×10^{-13}	1.72×10^{-14}	2.17×10^{6}	1.19×10^{5}	6.49	0.39	ND	ND	53,000	4800
573	GR08	2.27×10^{5}	2.78×10^{3}	3076	5.11×10^{-13}	2.59×10^{-14}	1.73×10^{6}	8.79×10^{4}	7.65	0.40	ND	ND	36,700	3200
591	GR08Rep	2.19×10^{5}	2.99×10^{3}	2040	4.34×10^{-13}	1.32×10^{-14}	1.38×10^{6}	4.20×10^{4}	6.31	0.21	ND	ND	ND	ND
573	GR09	6.39×10^{5}	7.28×10^{3}	2764	1.36×10^{-12}	3.57×10^{-14}	3.84×10^{6}	1.01×10^{5}	6.00	0.17	ND	ND	107,800	9500
582	GR10	8.74×10^{5}	1.47×10^{4}	2577	2.21×10^{-12}	5.54×10^{-14}	5.65×10^{6}	1.41×10^{5}	6.47	0.19	ND	ND	ND	ND
591	GR10Rep	8.61×10^{5}	1.04×10^{4}	1743	1.44×10^{-12}	3.18×10^{-14}	5.57×10^{6}	1.23×10^{5}	6.47	0.16	ND	ND	ND	ND
582	GR11	5.04×10^{5}	9.61×10^{3}	5545	4.02×10^{-13}	1.83×10^{-14}	2.89×10^{6}	1.32×10^{5}	5.73	0.28	ND	ND	ND	ND
583	GR12	1.25×10^{6}	2.71×10^{4}	3382	2.03×10^{-12}	4.85×10^{-14}	7.36×10^{6}	1.76×10^{5}	5.88	0.19	ND	ND	ND	ND

Note: TMMS—Tussey Mountain midslope; LRVF—Leading Ridge valley floor; LRMS—Leading Ridge midslope; LRRT—Leading Ridge ridgetop. ND—not determined (no ^{26}Al analyses performed). Rep—replicates: For replicates, a mean blank ratio ^{10}Be/^{9}Be = $1.19 \times 10^{-15} \pm 1.95 \times 10^{-16}$ was used to correct for background, and a mean blank ratio ^{26}Al/^{27}Al = $2.49 \times 10^{-14} \pm 1.90 \times 10^{-15}$ was used to correct for background.

*World Geodetic System 1984 (WGS 1984).

†Mean catchment elevation (asl—above sea level).

§Depth below drilling surface at elevation 0 m.

#Constant spallogenic production rate model; scaling scheme for spallation is from Lal (1991) and Stone (2000).

**A density of 2.7 g cm^{-3} was used for orthoquartzitic sandstone.

††Isotope ratios were normalized to ^{10}Be standards prepared by Nishiizumi et al. (2007) with a value of 2.85×10^{12} and using a ^{10}Be half-life of 1.39×10^{6} yr.

§§Uncertainties are reported at 1σ.

##A mean blank ratio ^{10}Be/^{9}Be = $1.20 \times 10^{-15} \pm 6.56 \times 10^{-16}$ was used to correct for background.

***Sample ratios for ^{26}Al were normalized to standard KNSTD with an assumed ratio of 1.818×10^{-12} (Nishiizumi, 2004).

†††A mean blank ratio ^{26}Al/^{27}Al = $1.97 \times 10^{-14} \pm 9.76 \times 10^{-15}$ was used to correct for background.

###Beryllium-10 model ages and erosion rates were calculated with the Cosmic-Ray Produced Nuclide Systematics (CRONUS) Earth online calculator (Balco et al., 2008), version 2.3, constants version 2.1.1, using global production rates (http://hess.ess.washington.edu/).

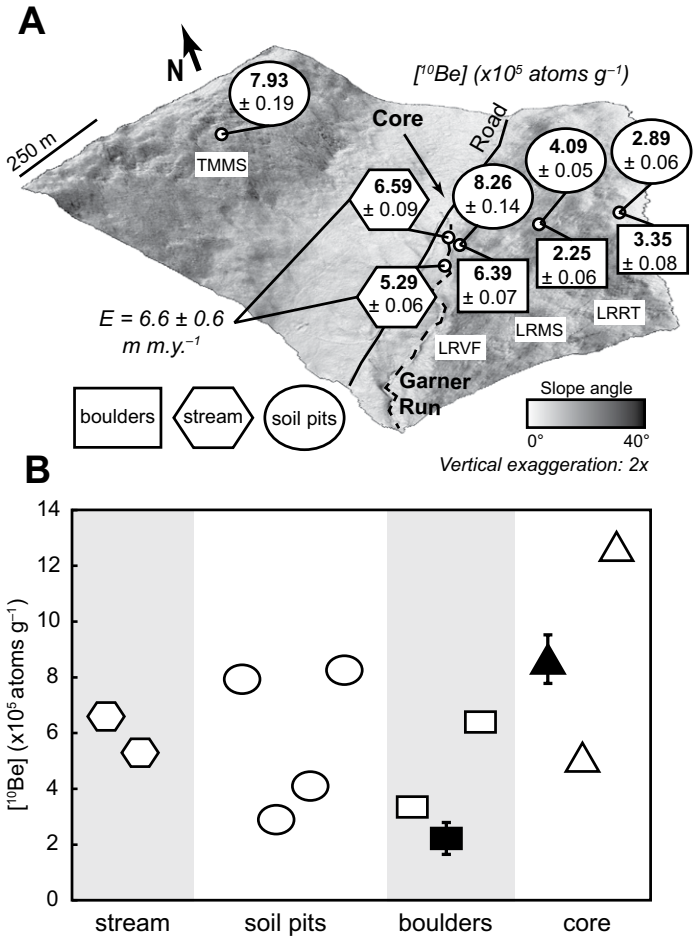

Figure 7. Overview of cosmogenic nuclide data. (A) Summary of ^{10}Be concentrations in samples collected from soil pits (circles), surface boulders (rectangles), and stream sediments (hexagons), shown on perspective slope-shade model of Garner Run subcatchment. Erosion rate, *E*, indicates average of two stream sediment samples. (B) Plot showing similarity in ^{10}Be concentrations of surface samples (same symbols as A). Also shown are ^{10}Be concentrations of core samples (triangles). Black symbols indicate samples with replicate measurements. Error bars (1σ or 1 standard error [SE] for replicate samples) are smaller than symbols where not shown. TMMS—Tussey Mountain midslope; LRVF—Leading Ridge valley floor; LRMS—Leading Ridge midslope; LRRT—Leading Ridge ridgetop.

pattern. The mean ^{10}Be concentration from two stream sediment samples ($6.0 \pm 0.5 \times 10^5$ atoms g^{-1}, ± 1 standard error [SE]) is similar to the mean of all soil and amalgamated surface boulder samples ($5.0 \pm 0.9 \times 10^5$ atoms g^{-1}, ±1 SE) and indicates a catchment-average hillslope lowering rate of 6.6 ± 0.6 m m.y.$^{-1}$, assuming steady erosion over and reflecting an integration time scale of ~100 k.y.

The mean ratio of ^{26}Al to ^{10}Be in the three amalgamated surface boulder samples is 6.5 ± 0.5 (±1 SE), indicating that the nuclide concentrations primarily reflect exposure (i.e., burial was either minor, shallow, or early on). Assuming the clasts recovered during coring were buried with an initial ^{26}Al/^{10}Be ratio of 6.5, consistent with the average of modern surface boulders, the lower two clasts (GR11 and GR12) show evidence of burial (lowered ^{26}Al/^{10}Be), whereas the ^{26}Al/^{10}Be ratio of the uppermost clast (GR10) is indistinguishable from the ^{26}Al/^{10}Be ratio of amalgamated surface boulders (Fig. 8).

Constraining Colluvial-Fill History

Based on topographic analysis and core observations, we estimate a total colluvial-fill volume of $9 \pm 5 \times 10^5$ m^3 in the Garner Run subcatchment (Fig. 9). Assuming that the source area for this material is limited to the adjacent slopes of Tussey Mountain and Leading Ridge, our colluvial-fill estimate is equivalent to 2 ± 1 m of hillslope lowering, and thus a minimum age of 300 ± 150 ka, assuming a long-term erosion rate of 6.6 ± 0.6 m m.y.$^{-1}$ (based on ^{10}Be in stream sediment) and no sediment evacuation.

Our 1-D modeling of ^{26}Al/^{10}Be ratios in the core provides an independent constraint on the age and history of the colluvial fill in Garner Run. For the single-burial scenario, no common history can explain at once all three buried clast ratios (Fig. 10). The lower two clasts require significant burial (210 ka ± 70 ka for the bottom sample [GR12] and 270 ka ± 110 ka for the middle sample [GR11], based on 1σ analytical error on the ^{26}Al/^{10}Be ratio), but the uppermost clast (GR10) has an ^{26}Al/^{10}Be ratio indistinguishable from the amalgamated surface boulder samples. Based on the 1σ analytical error on ^{26}Al/^{10}Be ratio, the upper sample requires a burial age <80 ka. Similar to the single-burial scenario, there is no consistent accumulation rate for the steady accumulation rate scenario (Fig. 10B) that explains the ^{26}Al/^{10}Be ratio of all three buried samples.

For the pulsed burial scenario (Fig. 10C), we modeled a two-stage burial history consisting of deposition of the lower 2.6 m of fill (spanning the two lower samples and fill between the middle and upper sample, at final depths of 6.5–3.9 m) in a single pulse, followed by a hiatus and then deposition of the upper 3.9 m in a second pulse, including the upper clast. We initially constrained the depth of the hiatus to between 4.7 and 3.4 m depth based on postburial production constraints from the low absolute concentrations of ^{10}Be and ^{26}Al in the middle clast, and then we refined the depth further to 3.9 m based on the final timing scenario (see the Data Repository [footnote 1]). The younger pulse of sediment deposition, t_1, cannot be dated but is constrained to <80 ka, as the ^{26}Al/^{10}Be ratio measured in the uppermost core clast is the same within uncertainty as that measured in amalgamated boulder samples from the slopes above. Depending on the value of t_1 (0–80 ka), the ^{26}Al/^{10}Be ratios measured in the lower two core samples are consistent (within 1σ) with a burial age of 420–260 ka, and thus we interpret t_0 = 340 ka ± 80 ka (Fig. 10C). We also show in Figure 10C a scenario where we assume t_1 corresponds to the transition to warmer conditions after the LGM (t_0 = 340 ka; t_1 = 16 ka), which we used to explore the sensitivity of our results to changes in N^{inh}_{10Be}, $R_{26/10}$, and the depth of the hiatus surface (see the Data Repository [footnote 1]).

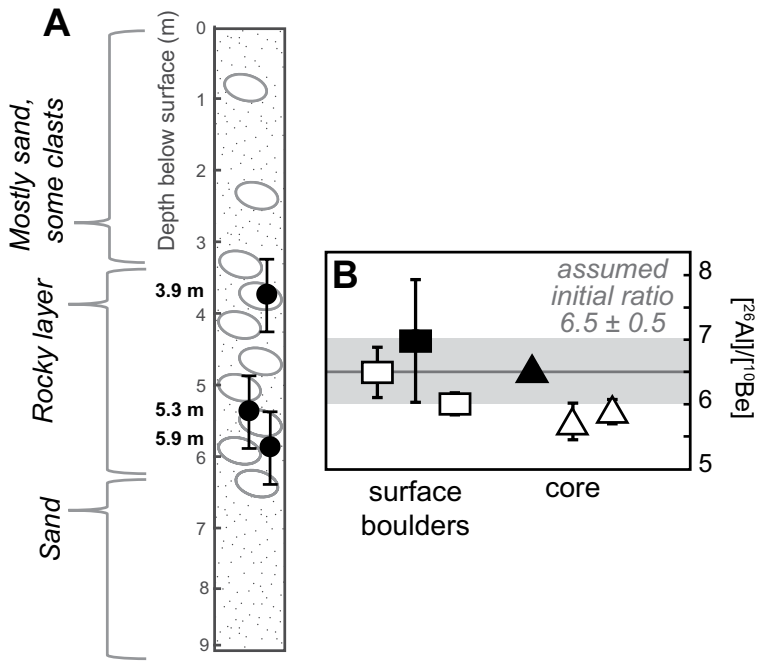

Figure 8. (A) Overview of HV1 core, showing location of samples taken at depths of 3.9 ± 0.5 m, 5.3 ± 0.5 m, and 5.9 ± 0.5 m below the surface. The interval between 3.4 and 6.4 m is a discrete rocky layer, overlying sand between 9.1 and 6.4 m depth and covered by a mix of sand and two clasts from unknown depths from 3.4 to 0 m below the surface. (B) Plot showing measured $^{26}Al/^{10}Be$ ratio for surface clasts and core samples (same symbols as Fig. 7).

DISCUSSION

Controls on Spatial Variability in Regolith Texture

Our surface mapping of regolith texture provides a framework for both interpreting the history of periglacial surface processes at Garner Run and assessing how these processes were controlled by topographic slope and aspect. Broadly, our mapping indicates a pattern of boulder fields more widespread in size and frequency near ridgelines and finer-grained regolith mantling the low-sloping valley floor. Where slides and slumps are expressed in the lidar topography, we similarly observed a pattern of open or canopied boulder fields exposed in the scar, and a mixture of soil and boulders in the deposit. We interpret boulder fields as a lag of coarse material left behind after downslope transport of finer-grained material via solifluction or active layer detachment, consistent with modern periglacial landscapes, where these processes are promoted by the presence of a fine-grained matrix (Matsuoka, 2001; French, 2013). Additionally, the observed thinning of E horizons in soils with distance downslope is consistent with subsurface eluviation of clays within solifluction lobes (Carter and Ciolkosz, 1986). We interpret the boulder fields as areas

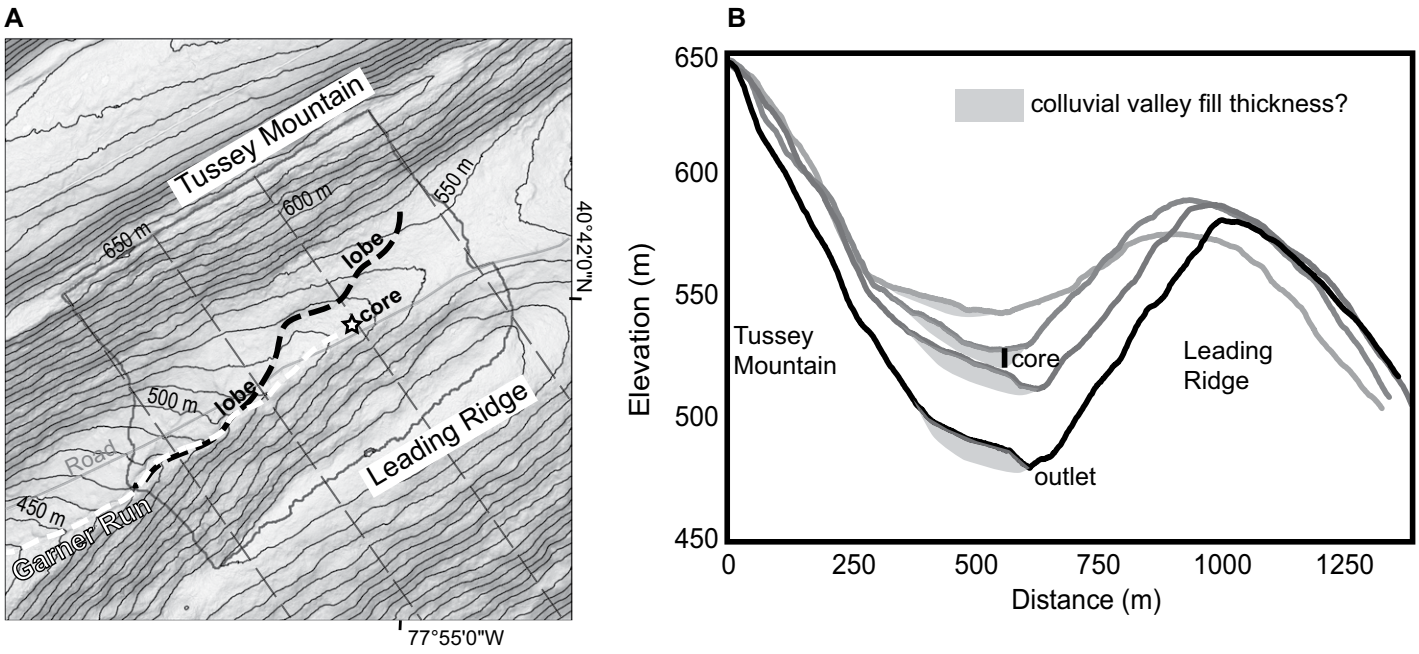

Figure 9. (A) Shaded relief map and (B) topographic and core-constrained estimates of colluvial valley-fill thickness. Based on topographic cross sections, we project only minimum (5 m) long-term stored valley fill at the northeastern drainage divide, where solifluction lobes and bench are least pronounced. Minimum fill thickness of 9 m is constrained by core location for one cross section. Note that major lobe feature in shaded relief map (dashed line in A) does not reach core location. Downstream, field observations indicate stream incises through ~5 m of lobe material.

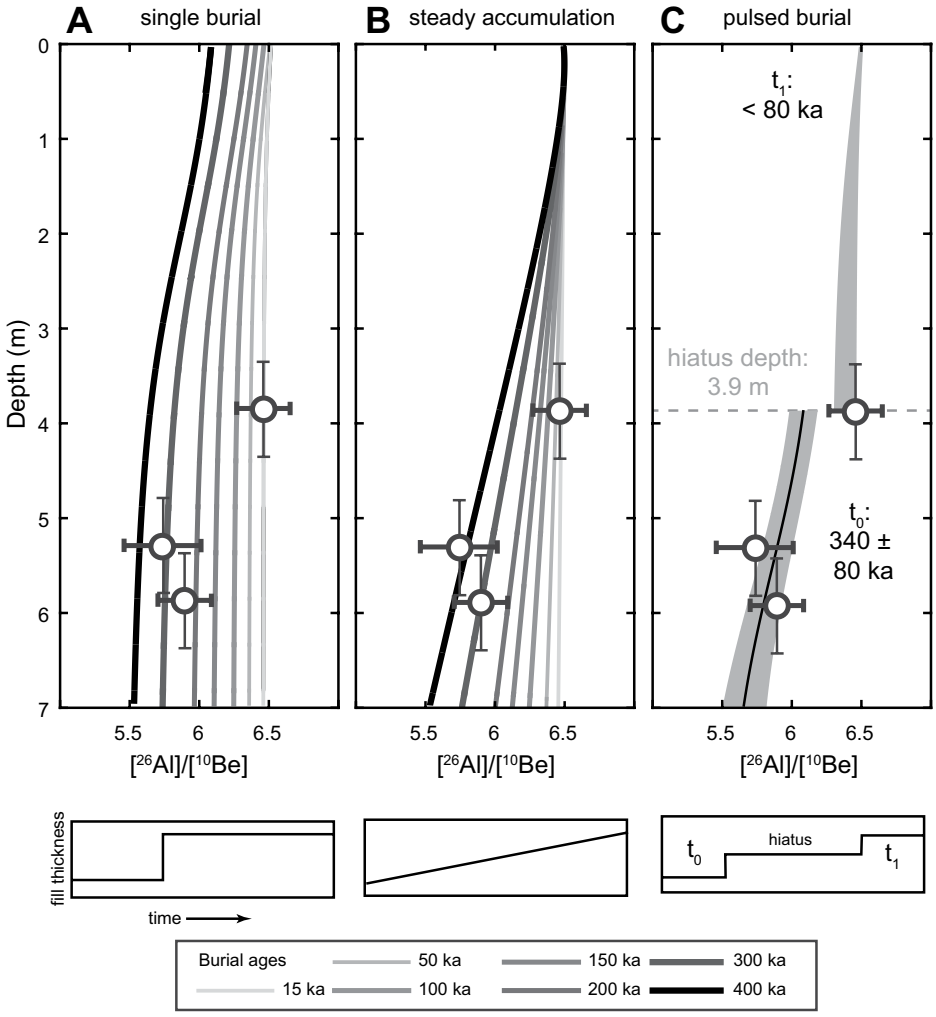

Figure 10. Comparison of measured vs. predicted $^{26}Al/^{10}Be$ ratios as a function of depth for HV1 drill core samples. (A) Single burial scenario, showing contours of deposition age, t_0, in ka. (B) Steady accumulation scenario, showing contours of start of deposition, t_0, in ka. (C) Pulsed burial scenario, showing range of two-staged burial models consistent with data (t_0 = 340 ± 80 ka; t_1 < 80 ka) and example model assuming t_1 is Last Glacial Maximum in age (solid line; t_0 = 340 ka; t_1 = 16 ka), assuming uniform N^{inh}_{10Be} = 4 × 10^5 atoms g^{-1}.

in the landscape where regolith is thinnest and bedrock is closest to the surface. For example, linear transects of open boulder fields that parallel the strike of the underlying bedrock (Fig. 3) are composed of blocks that are similar in size and shape (Fig. 6A) to those adjacent to in-place bedrock along ridgelines (Fig. 2), suggesting a local origin.

We observed a decrease in the median boulder size with increased interstitial soil content, and a decrease in median boulder size with distance from the ridgeline that also corresponds to spatial patterns in surface cover type (Figs. 3 and 5). The observations at Garner Run (Fig. 5) are consistent with regional observations of downslope patterns in boulder size, rounding, and weathering rind development (Gentoso, 2008), and they may reflect one of two end-member scenarios: (1) Boulders are produced from bedrock during periglacial conditions and then decrease in size during downslope transport, or (2) variations in boulder size reflect a pre-Pleistocene weathering profile that has been progressively stripped by periglacial processes (F. Pazzaglia, 2017, personal commun.). Cosmogenic nuclide concentrations in soils increase with distance downslope on Leading Ridge (Fig. 7), but they are not suited for distinguishing among the two scenarios. Similarly, the sandy fill observed in the HV1 drill core (Fig. 8) may reflect the unroofing of finer-grained regolith, or it may be the by-product of in situ weathering of coarser -grained material.

The most prominent pattern in regolith texture that we observed at Garner Run is a strong asymmetry in boulder cover, with boulder fields (both canopied and open) covering the southeast-facing slope of Tussey Mountain, and more extensive soil cover on the northwest-facing slope of Leading Ridge (Fig. 3). In the low-sloping valley floor, the topographic expression of lobe features (Fig. 1B) and the pinning of the stream against the base of Leading Ridge (Fig. 3) suggest that the colluvial fill is sourced primarily from periglacial solifluction of material from Tussey Mountain, a result consistent with regional observations of solifluction lobes concentrated at the toe slopes of southeast-facing hillslopes (Fig. 1A). Although this pattern suggests an aspect control on periglacial hillslope erosion and sediment transport, the southeast-facing slope of Tussey Mountain is steeper than the northwest-facing slope of Leading Ridge (Fig. 3). Additionally, as Leading Ridge steepens to the southwest, regolith texture transitions from mainly fine-grained soil to extensive canopied boulder fields. Thus, at Garner Run, it is unclear how much of the pattern in hillslope erosion and regolith texture is due to differences in aspect-controlled microclimate versus structurally controlled topographic slope. Additional analysis and mapping of nearby catchments with similar lithology but differing topography are needed to untangle these competing controls on periglacial landscape evolution.

Colluvial-Fill History and Implications for Hillslope-Channel Coupling

Our preferred model of colluvial-fill history for interpreting the $^{26}Al/^{10}Be$ ratios from buried clasts is a two-staged pulsed accumulation, with material from 6.4 to 3.9 m depth deposited at 340 ± 80 ka, a hiatus until at least 80 ka, and then a more recent pulse that deposited the upper 3.9 m of colluvium. This is the simplest model that explains our data from the core and is consistent with our independent minimum age estimate of 300 ± 150 ka for the colluvial fill above 6.4 m depth, based on fill volume and ^{10}Be-derived erosion rates. Since there is at least an additional 2.7 m of fill below our lowest core sample (Fig. 8), the age of 340 ± 80 ka is a minimum estimate of the oldest colluvial fill in Garner Run. Thus, the headwater valley of Garner Run preserves a sedimentary record that spans multiple glacial cycles as a consequence of slow hillslope erosion rates and limited evacuation of material from the valley axis.

In contrast to surficial observations in the Garner Run valley bottom of clayey soils and boulders embedded in a fine-grained matrix

(Fig. 3), core observations show only sand and larger clasts, with an absence of clay. Because the core is along the valley axis, it is possible that winnowing of finer material occurred during depositional hiatuses through surface or subsurface flow. The modern stream at Garner Run generally lacks particles finer than sand size (see the Data Repository [footnote 1]), and there is considerable subsurface flow in the valley fill, based on field observations of audible flowing water in the subsurface and evidence for hyporheic exchange in surface-water chemistry (Hoagland et al., 2017). Interglacial winnowing is also consistent with our modeled hiatus depth of 3.9 m, as this depth corresponds to a textural change in our core from mostly large clasts below to a mix of fine-grained material and clasts above.

The long-lived preservation of colluvial fill in the valley floor of Garner Run is likely a consequence of the underlying lithology and upland position insulated from regional base level. Because the Tuscarora Formation weathers as large, resistant blocks of quartz sandstone, material delivered to the channel network armors the channel and is not readily transported until the blocks weather in place sufficiently, either through frost cracking, abrasion, or dissolution. Additionally, due to its location upstream of a knickpoint (Fig. 1A), Garner Run is isolated from regional base level and exhibits low channel steepness and slow erosion rates compared to nearby catchments downstream of the knickpoint (Miller et al., 2013; Brantley et al., 2016), limiting the ability of the stream to evacuate the colluvial valley fill in Garner Run during interglacial periods.

Regionally, both the time scale of sediment storage and direct transfer of hillslope debris to burial in valleys make sedimentary records in central Appalachian headwater valleys valuable archives for assessing the interplay of hillslope-channel coupling throughout the Pleistocene, and understanding climate controls on landscape evolution. The lithologic and structural control on periglacial debris storage, demonstrated here at Garner Run, implies that structural traps, which are common within tightly folded sandstone units in the Valley and Ridge, can facilitate thick (tens of meters) colluvial sediment accumulation in headwater catchments. Because regionally extensive sandstone units like the Tuscarora Formation span a wide latitudinal gradient in the unglaciated Appalachians, there is potential to explore how paleoclimate gradients control the pattern and pace of hillslope erosion, particularly if colluvial sedimentation records preserve independent climate proxies or paleoenvironmental indicators.

Implications for the Evolution of the Critical Zone

Our results highlight how the regolith mantling Garner Run both records past critical zone processes and influences the structure and composition of the modern critical zone. The persistence of regolith at Garner Run means that the critical zone at this site integrates multiple climate cycles, which set boundary conditions like moisture, temperature, and biota that in turn control the pace and pattern of critical zone processes (Anderson et al., 2007; Brantley and Lebedeva, 2011). Previous work on Valley and Ridge periglacial features, drawing on radiocarbon and sediment thermoluminescence ages, assigned Wisconsinan (LGM) ages to colluvial soils overlying reddened pre-Wisconsinan soils (Clark and Ciolkosz, 1988; Ciolkosz et al., 1990), and work at the nearby Shale Hills catchment shows regolith postdates the LGM (West et al., 2013). However, the regolith at Garner Run has an older and more complex exposure history, and thus landforms may be composite features with nuanced erosional histories (e.g., Wilson et al., 2008; Denn et al., 2018). Soil properties are not just a function of modern pedogenesis, but also ancient sediment transport and cold-weather processes (Ciolkosz et al., 1990). Moreover, slow erosion rates facilitate the trapping of windborne dust (Cronce, 1988), a likely contributor to the nutrient-rich soils at Garner Run, which is underlain by an erosionally resistant orthoquartzite bedrock. Heterogeneity in the regolith and shallow subsurface, shaped by relict climate conditions, controls modern hydrology by modulating infiltration and subsurface flow paths and is thus an important consideration for hydrologic models (McDonnell et al., 2007; Shi et al., 2013), and important for interpretations of modern fluxes of mass and energy in the critical zone (Brantley and Lebedeva, 2011).

CONCLUSIONS

The widespread preservation of periglacial landforms in sandstone landscapes of central Pennsylvania indicates that cold-climate processes are the dominant mechanism for sediment production and downslope transport at Garner Run, with limited landscape modification by surface processes active during warmer climates. Coarse sediment armoring of channels and limited incision into the colluvial valley fills suggest that boulder-rich periglacial colluvium delivered to channels is not readily evacuated during interglacial periods. Consequently, and as indicated by sediment core observations and cosmogenic nuclide samples, the colluvial valley fill at Garner Run preserves a pulsed depositional record from multiple glacial cycles spanning at least 340 ± 80 k.y. Due to slow erosion rates, regolith on hillslopes integrates pre-LGM conditions—an assertion verified by relatively high concentrations of ^{10}Be measured in hillslope regolith. Our field and topographic analyses show that periglaciation at Garner Run exerts a primary control on spatial patterns in regolith texture and critical zone architecture, and thus modern critical zone processes.

ACKNOWLEDGMENTS

We thank S. Granke, C. Martin, and P. Silverhart for field and geographic information system (GIS) assistance, and S.L. Brantley, D.J. Merritts, and F.J. Pazzaglia for thoughtful discussion. J. Marshall and F.J. Pazzaglia provided constructive reviews that helped improve the paper. This work was supported by the National Science Foundation Critical Zone Observatories program (grant EAR-13-31726) and a Marie Morisawa Research Award to J. Del Vecchio through the Quaternary Geology and Geomorphology Division of the Geological Society of America. Field work was conducted in Rothrock State Forest, which is funded and managed by the Pennsylvania Department of Conservation and Natural Resources, Bureau of Forestry. PRIME Laboratory and M.W. Caffee acknowledge support from the National Science Foundation (EAR-1153689). Lidar data acquisition and processing were completed by the National Center for Airborne Laser Mapping (NCALM), funded by the National Science Foundation Award EAR-0922307, and coordinated by Q. Guo for the Susquehanna Shale Hills Critical Zone Observatory funded by the National Science Foundation Award EAR-0725019 (https://doi.org/10.5069/G9VM496T).

REFERENCES CITED

Anderson, R.S., Anderson, S.P., and Tucker, G.E., 2013, Rock damage and regolith transport by frost: An example of climate modulation of the geomorphology of the critical zone: Earth Surface Processes and Landforms, v. 38, no. 3, p. 299–316, https://doi.org/10.1002/esp.3330.

Anderson, S.P., von Blanckenburg, F., and White, A.F., 2007, Physical and chemical controls on the critical zone: Elements, v. 3, no. 5, p. 315–319, https://doi.org/10.2113/gselements.3.5.315.

Argento, D.C., Stone, J.O., Reedy, R.C., and O'Brien, K., 2015, Physics-based modeling of cosmogenic nuclides part II—Key aspects of in-situ cosmogenic nuclide production: Quaternary Geochronology, v. 26, no. 1, p. 44–55, https://doi.org/10.1016/j.quageo.2014.09.005.

Balco, G., Stone, J.O., Lifton, N.A., and Dunai, T.J., 2008, A complete and easily accessible means of calculating surface exposure ages or erosion rates from ^{10}Be and ^{26}Al measurements: Quaternary Geochronology, v. 3, no. 3, p. 174–195, https://doi.org/10.1016/j.quageo.2007.12.001.

Brantley, S.L., and Lebedeva, M., 2011, Learning to read the chemistry of regolith to understand the critical zone: Annual Review of Earth and Planetary Sciences, v. 39, no. 1, p. 387–416, https://doi.org/10.1146/annurev-earth-040809-152321.

Brantley, S.L., Dibiase, R., Russo, T., Shi, Y., Lin, H., Davis, K.J., and Kaye, M., 2016, Designing a suite of measurements to understand the critical zone: Earth Surface Dynamics, v. 4, p. 211–235, https://doi.org/10.5194/esurf-4-211-2016.

Braun, D.D., 1989, Glacial and periglacial erosion of the Appalachians: Geomorphology, v. 2, no. 1-3, p. 233–256, https://doi.org/10.1016/0169-555X(89)90014-7.

Brush, L.M., Jr., 1961, Drainage Basins, Channels, and Flow Characteristics of Selected Streams in Central Pennsylvania: U.S. Geological Survey Professional Paper 282-F, p. 145–181.

Bunte, K., and Abt, S.R., 2001, Sampling Surface and Subsurface Particle-Size Distributions in Wadable Gravel- and Cobble-Bed Streams for Analyses in Sediment Transport, Hydraulics, and Streambed Monitoring: U.S. Department of Agriculture, Forest Service, Rocky Mountain Research Station General Technical Report RMRS-GTR-74, 428 p.

Carter, B.J., and Ciolkosz, E.J., 1986, Sorting and thickness of waste mantle material on a sandstone spur in central Pennsylvania: Catena, v. 13, no. 3, p. 241–256, https://doi.org/10.1016/0341-8162(86)90001-9.

Chmeleff, J., von Blanckenburg, F., Kossert, K., and Jakob, D., 2010, Determination of the ^{10}Be half-life by multicollector ICP-MS and liquid scintillation counting: Nuclear Instruments & Methods in Physics Research, Section B, Beam Interactions with Materials and Atoms, v. 268, no. 2, p. 192–199, https://doi.org/10.1016/j.nimb.2009.09.012.

Ciolkosz, E.J., Carter, B.J., Hoover, M.T., Cronce, R.C., Waltman, W.J., and Dobos, R.R., 1990, Genesis of soils and landscapes in the Ridge and Valley Province of central Pennsylvania: Geomorphology, v. 3, no. 3-4, p. 245–261, https://doi.org/10.1016/0169-555X(90)90006-C.

Ciolkosz, E.J., Drohan, P., and Sevon, W., 2008, The Pleistocene record in the middle and lower Susquehanna River Basin and the longer term evolution of the Susquehanna Basin landscape, *in* Braun, D., ed., 20th Biennial Meeting of the American Quaternary Association: University Park, Pennsylvania, American Quaternary Association Field Trip Guide, p. 1–58.

Clark, G.M., and Ciolkosz, E.J., 1988, Periglacial geomorphology of the Appalachian highlands and interior highlands south of the glacial border—A review: Geomorphology, v. 1, no. 3, p. 191–220, https://doi.org/10.1016/0169-555X(88)90014-1.

Clark, G.M., Behling, R.E., Braun, D.D., Ciolkosz, E.J., Kite, J.S., and Marsh, B., 1992, Central Appalachian Periglacial Geomorphology: Pennsylvania State University Agronomy Series Publication 120, 248 p.

Corbett, L.B., Bierman, P.R., and Rood, D.H., 2016, An approach for optimizing in situ cosmogenic ^{10}Be sample preparation: Quaternary Geochronology, v. 33, p. 24–34, https://doi.org/10.1016/j.quageo.2016.02.001.

Corbett, L.B., Bierman, P.R., Rood, D.H., Caffee, M.W., Lifton, N.A., and Woodruff, T.E., 2017a, Cosmogenic ^{26}Al/^{10}Be surface production ratio in Greenland: Geophysical Research Letters, v. 44, no. 3, p. 1350–1359, https://doi.org/10.1002/2016GL071276.

Corbett, L.B., Bierman, P.R., Stone, B.D., Caffee, M.W., and Larsen, P.L., 2017b, Cosmogenic nuclide age estimate for Laurentide ice sheet recession from the terminal moraine, New Jersey, USA, and constraints on latest Pleistocene ice sheet history: Quaternary Research, v. 87, no. 3, p. 482–498, https://doi.org/10.1017/qua.2017.11.

Cronce, R.C., 1988, The Genesis of Soils Overlying Dolomite in the Nittany Valley of Central Pennsylvania [Ph.D. thesis]: University Park, Pennsylvania, Pennsylvania State University, 388 p.

Denn, A.R., Bierman, P.R., Zimmerman, S.R.H., Caffee, M.W., Corbett, L.B., and Kirby, E., 2018, Cosmogenic nuclides indicate that boulder fields are dynamic, ancient, multigenerational features: GSA Today, v. 28, https://doi.org/10.1130/GSATG340A.1.

DiBiase, R., Del Vecchio, J., Mount, G., Hayes, J.L., Comas, X., Guo, L., Lin, H., Zarif, F., Forsythe, B., and Brantley, S.L., 2016, Quantifying the spatial variability in critical zone architecture through surface mapping and near-surface geophysics: San Francisco, California, American Geophysical Union, Fall meeting supplement, abstract EP41F-01.

Flueckinger, L.A., 1969, Geology of a Portion of the Allensville Quadrangle, Centre and Huntingdon Counties, Pennsylvania: Bureau of Topographic and Geologic Survey, Commonwealth of Pennsylvania State Planning Board Report 176, scale 1:24,000.

French, H.M., 2013, The Periglacial Environment (3rd ed.): Chichester, UK, John Wiley and Sons Ltd., 458 p.

Gardner, T.W., Ritter, J.B., Shuman, C.a., Bell, J.C., Sasowsky, K.C., and Pinter, N., 1991, A periglacial stratified slope deposit in the Valley and Ridge Province of central Pennsylvania, USA: Sedimentology, stratigraphy, and geomorphic evolution: Permafrost and Periglacial Processes, v. 2, p. 141–162, https://doi.org/10.1002/ppp.3430020208.

Gentoso, M., 2008, Boulder Fields of the Tuscarora Formation [B.S. thesis]: University Park, Pennsylvania State University, 70 p.

Granger, D.E., and Muzikar, P.F., 2001, Dating sediment burial with in situ–produced cosmogenic nuclides: Theory, techniques, and limitations: Earth and Planetary Science Letters, v. 188, no. 1-2, p. 269–281, https://doi.org/10.1016/S0012-821X(01)00309-0.

Granger, D.E., and Riebe, C.S., 2014, Cosmogenic Nuclides in Weathering and Erosion, *in* Holland, H., and Turekian, K., Treatise on Geochemistry, Volume 5: Surface and Ground Water, Weathering, and Soils (2nd Edition): Amsterdam, Elsevier Ltd., p. 401–436https://doi.org/10.1016/B978-0-08-095975-7.00514-3.

Hales, T.C., and Roering, J.J., 2007, Climatic controls on frost cracking and implications for the evolution of bedrock landscapes: Journal of Geophysical Research–Earth Surface, v. 112, no. 2, F02033, https://doi.org/10.1029/2006JF000616.

Hallet, B., Hunter, L., and Bogen, J., 1996, Rates of erosion and sediment evacuation by glaciers: A review of field data and their implications: Global and Planetary Change, v. 12, no. 1-4, p. 213–235, https://doi.org/10.1016/0921-8181(95)00021-6.

Hoagland, B., Russo, T.A., Gu, X., Hill, L., Kaye, J., Forsythe, B., and Brantley, S.L., 2017, Hyporheic zone influences on concentration-discharge relationships in a headwater sandstone stream: Water Resources Research, v. 53, p. 4643–4667, https://doi.org/10.1002/2016WR019717.

Hoover, M.T., and Ciolkosz, E.J., 1988, Colluvial soil parent material relationships in the ridge and valley physiographic province of Pennsylvania: Soil Science, v. 145, no. 3, p. 163–172.

Jungers, M.C., Bierman, P.R., Matmon, A., Nichols, K., Larsen, J., and Finkel, R., 2009, Tracing hillslope sediment production and transport with in situ and meteoric ^{10}Be: Journal of Geophysical Research–Earth Surface, v. 114, no. 4, F04020, https://doi.org/10.1029/2008JF001086.

Kneller, M., and Peteet, D., 1999, Late-Glacial to early Holocene climate changes from a central Appalachian pollen and macrofossil record: Quaternary Research, v. 51, p. 133–147, https://doi.org/10.1006/qres.1998.2026.

Kohl, C.P., and Nishiizumi, K., 1992, Chemical isolation of quartz for measurement of in-situ–produced cosmogenic nuclides: Geochimica et Cosmochimica Acta, v. 56, no. 9, p. 3583–3587, https://doi.org/10.1016/0016-7037(92)90401-4.

Koppes, M.N., and Montgomery, D.R., 2009, The relative efficacy of fluvial and glacial erosion over modern to orogenic timescales: Nature Geoscience, v. 2, no. 9, p. 644–647, https://doi.org/10.1038/ngeo616.

Kovar, A.J., 1965, Pollen analysis of the Bear Meadows Bog of central Pennsylvania: Proceedings of the Pennsylvania Academy of Science, v. 38, no. 2, p. 16–24.

Lal, D., 1991, Cosmic ray labeling of erosion surfaces: In situ nuclide production rates and erosion models: Earth and Planetary Science Letters, v. 104, no. 2-4, p. 424–439, https://doi.org/10.1016/0012-821X(91)90220-C.

Lewkowicz, A.G., and Harris, C., 2005, Frequency and magnitude of active-layer detachment failures in discontinuous and continuous permafrost, northern Canada: Permafrost and Periglacial Processes, v. 130, p. 115–130, https://doi.org/10.1002/ppp.522.

Matsuoka, N., 2001, Solifluction rates, processes and landforms: A global review: Earth-Science Reviews, v. 55, no. 1-2, p. 107–134, https://doi.org/10.1016/S0012-8252(01)00057-5.

McDonnell, J.J., Sivapalan, M., Vaché, K., Dunn, S., Grant, G., Haggerty, R., Hinz, C., Hooper, R., Kirchner, J., Roderick, M.L., Selker, J., and Weiler, M., 2007, Moving beyond heterogeneity and process complexity: A new vision for watershed hydrology: Water Resources Research, v. 43, no. 7, p. 1–6, https://doi.org/10.1029/2006WR005467.

Merritts, D.J., Walter, R.C., Blair, A., Demitroff, M., Potter, N., Jr., Alter, S., Markey, E., Guillorn, S., Gigliotti, S., and Studnicky, C., 2015, lidar, orthoimagery, and field analysis of periglacial landforms and their cold climate signature, unglaciated Pennsylvania and Maryland: Geological Society of America Abstracts with Programs, v. 47, no. 7, p. 831.

Miller, S.R., Sak, P.B., Kirby, E., and Bierman, P.R., 2013, Neogene rejuvenation of central Appalachian topography: Evidence for differential rock uplift from stream profiles and erosion rates: Earth and Planetary Science Letters, v. 369–370, p. 1–12, https://doi.org/10.1016/j.epsl.2013.04.007.

Nishiizumi, K., 2004, Preparation of ^{26}Al AMS standards: Nuclear Instruments and Methods in Physics Research, Section B, Beam Interactions with Materials and Atoms, v. 223–224, p. 388–392.

Nishiizumi, K., Imamura, M., Caffee, M.W., Southon, J.R., Finkel, R.C., and McAninch, J., 2007, Absolute calibration of ^{10}Be AMS standards: Nuclear Instruments & Methods in Physics Research, Section B, Beam Interactions with Materials and Atoms, v. 258, no. 2, p. 403–413, https://doi.org/10.1016/j.nimb.2007.01.297.

PAMAP Program, 2006, Pennsylvania Department of Conservation and Natural Resources: http://www.dcnr.state.pa.us/topogeo/pamap/lidar/index.htm (last accessed 1 July 2015).

Pizzuto, J.E., 1995, Downstream fining in a network of gravel-bedded rivers: Water Resources Research, v. 31, no. 3, p. 753–759, https://doi.org/10.1029/94WR02532.

Portenga, E.W., Bierman, P.R., Rizzo, D.M., and Rood, D.H., 2013, Low rates of bedrock outcrop erosion in the central Appalachian Mountains inferred from in situ ^{10}Be: Geological Society of America Bulletin, v. 125, no. 1-2, p. 201–215, https://doi.org/10.1130/B30559.1.

Ramage, J.M., Gardner, T.W., and Sasowsky, I.D., 1998, Early Pleistocene Glacial Lake Lesley, West Branch Susquehanna River valley, central Pennsylvania: Geomorphology, v. 22, p. 19–37, https://doi.org/10.1016/S0169-555X(97)00053-6.

Rempel, A.W., Marshall, J.A., and Roering, J.J., 2016, Modeling relative frost weathering rates at geomorphic scales: Earth and Planetary Science Letters, v. 453, p. 87–95, https://doi.org/10.1016/j.epsl.2016.08.019.

Robinson, G.R., 1959, Tree Mortality and Defects on the Leading Ridge Watershed Number One [M.S. thesis]: University Park, Pennsylvania, Pennsylvania State University, 50 p.

Shi, Y., Davis, K.J., Zhang, F., and Duffy, C.J., 2013, Development of a coupled land surface hydrologic model and evaluation at a critical zone observatory: Journal of Hydrometeorology, v. 14, p. 1401–1420, https://doi.org/10.1175/JHM-D-12-0145.1.

Shuman, B.N., and Marsicek, J., 2016, The structure of Holocene climate change in mid-latitude North America: Quaternary Science Reviews, v. 141, p. 38–51, https://doi.org/10.1016/j.quascirev.2016.03.009.

Shuman, B., Webb, T., Bartlein, P., and Williams, J.W., 2002, The anatomy of a climate oscillation: Vegetation change in eastern North America during the Younger Dryas chronozone: Quaternary Science Reviews, v. 21, p. 1777–1791, https://doi.org/10.1016/S0277-3791(02)00030-6.

Stone, J.O., 2000, Air pressure and cosmogenic isotope production: Journal of Geophysical Research, v. 105, no. B10, p. 23,753–23,759, https://doi.org/10.1029/2000JB900181.

Taber, S., 1929, Frost heaving: The Journal of Geology, v. 37, no. 5, p. 428–461, https://doi.org/10.1086/623637.

Thomas, E.M., Lin, H., Duffy, C.J., Sullivan, P.L., Holmes, G.H., Brantley, S.L., and Jin, L., 2013, Spatiotemporal patterns of water stable isotope compositions at the Shale Hills Critical Zone Observatory: Linkages to

subsurface hydrologic processes: Vadose Zone Journal, v. 12, no. 4, https://doi.org/10.2136/vzj2013.01.0029.

Soil Survey Staff, 2014, Soil survey field and laboratory methods manual: Soil Survey Investigations Report no. 51, vesion 2.0: Lincoln, Nebraska, U.S. Department of Agriculture, Natural Resources Conservation Service, 457 p.

Vandenberghe, J., French, H.M., Gorbunov, A., Marchenko, S., Velichko, A.A., Jin, H., Cui, Z., Zhang, T., and Wan, X., 2014, The Last Permafrost Maximum (LPM) map of the Northern Hemisphere: Permafrost extent and mean annual air temperatures, 25–17ka BP: Boreas, v. 43, no. 3, p. 652–666, https://doi.org/10.1111/bor.12070.

Watts, W.A., 1979, Late Quaternary vegetation of central Appalachia and the New Jersey coastal plain: Ecological Monographs, v. 49, no. 4, p. 427–469, https://doi.org/10.2307/1942471.

West, N., Kirby, E., Bierman, P., Slingerland, R., Ma, L., Rood, D., and Brantley, S., 2013, Regolith production and transport at the Susquehanna Shale Hills Critical Zone Observatory, part 2: Insights from meteoric ^{10}Be: Journal of Geophysical Research–Earth Surface, v. 118, no. 3, p. 1877–1896, https://doi.org/10.1002/jgrf.20121.

Westoby, M.J., Brasington, J., Glasser, N.F., Hambrey, M.J., and Reynolds, J.M., 2012, "Structure-from-motion" photogrammetry: A low-cost, effective tool for geoscience applications: Geomorphology, v. 179, p. 300–314, https://doi.org/10.1016/j.geomorph.2012.08.021.

Williams, J.W., Shuman, B.N., Webb, T., Bartlein, P.J., and Leduc, P.L., 2004, Late-Quaternary vegetation dynamics in North America: Scaling from taxa to biomes: Ecological Monographs, v. 74, no. 2, p. 309–334, https://doi.org/10.1890/02-4045.

Wilson, P., Bentley, M.J., Schnabel, C., Clark, R., and Xu, S., 2008, Stone run (block stream) formation in the Falkland Islands over several cold stages, deduced from cosmogenic isotope (^{10}Be and ^{26}Al) surface exposure dating: Journal of Quaternary Science, v. 23, no. 5, p. 461–473, https://doi.org/10.1002/jqs.1156.

Yoo, K., Weinman, B., Mudd, S.M., Hurst, M., Attal, M., and Maher, K., 2011, Evolution of hillslope soils: The geomorphic theater and the geochemical play: Applied Geochemistry, v. 26, supplement, p. S149–S153, https://doi.org/10.1016/j.apgeochem.2011.03.054.

Science Editor: Bradley S. Singer

Manuscript Received 17 August 2017
Revised Manuscript Received 8 January 2018
Manuscript Accepted 26 February 2018

Printed in the USA